Redox Biology 47 (2021) 102128

Contents lists available at ScienceDirect

Redox Biology

journal homepage: www.elsevier.com/locate/redox

TMBIM6 regulates redox-associated posttranslational modifications of IRE1α and ER stress response failure in aging mice and humans

Kashi Raj Bhattarai [a,d,1], Hyun-Kyoung Kim [a,1], Manoj Chaudhary [b], Mohammad Mamun Ur Rashid [b], Jisun Kim [a], Hyung-Ryong Kim [c,*], Han-Jung Chae [a,**]

[a] School of Pharmacy and Institute of New Drug Development, Jeonbuk National University, 54896, Jeonju, Republic of Korea
[b] Department of Pharmacology and Institute of New Drug Development, Jeonbuk National University Medical School, 54896, Jeonju, Republic of Korea
[c] Department of Dental Pharmacology, College of Dentistry, Jeonbuk National University, Jeonju, 54896, Republic of Korea
[d] Department of Pharmaceutical Sciences, St. Jude Children's Research Hospital, 38105, Memphis, TN, USA

ARTICLE INFO

Keywords:
TMBIM6/BI-1
Aging
IRE1α modifications
S-nitrosylation
Sulfonation
ER stress response failure

ABSTRACT

Age-associated persistent ER stress is the result of declining chaperone systems of the ER that reduces cellular functions, induces apoptosis, and leads to age-related diseases. This study investigated the previously unknown regulatory mechanism of TMBIM6 during age-associated hepatic abnormalities. Wild-type (WT) and the TMBIM6 knockout (TMBIM6$^{-/-}$) mice liver, human liver samples from different age groups were used to demonstrate the effect of physiological aging on liver. For TMBIM6 rescue experiments, TMBIM6$^{-/-}$ old mice and stable human hepatic cell lines expressing TMBIM 6 were used to study the functional role of TMBIM6 on aging-associated steatosis and its associated mechanisms. In aging humans and mice, we observed declined expression of TMBIM6 and aberrant UPR expression, which were associated with high hepatic lipid accumulation. During aging, TMBIM6-deficient mice had increased senescence than their WT counterparts. We identified redox-mediated posttranslational modifications of IRE1α such as S-nitrosylation and sulfonation were higher in TMBIM6-deficient aging mice and humans, which impaired the ER stress response signaling. Sulfonation of IRE1α enhanced regulated IRE1α-dependent decay (RIDD) activity inducing TMBIM6 decay, whereas S-nitrosylation of IRE1α inhibited XBP1 splicing enhancing the cell death. Moreover, the degradation of miR-338-3p by strong IRE1α cleavage activity enhanced the expression of PTP1B, resulting in diminishing phosphorylation of PERK. The re-expression of TMBIM6 reduced IRE1α modifications, preserved ER homeostasis, reduced senescence and senescence-associated lipid accumulation in human hepatic cells and TMBIM6-depleted mice. S-nitrosylation or sulfonation of IRE1α and its controller, the TMBIM6, might be the potential therapeutic targets for maintaining ER homeostasis in aging and aging-associated liver diseases.

1. Introduction

The endoplasmic reticulum (ER) is vital to multiple cellular functions such as synthesis and folding of proteins, and transportation of synthesized proteins [1]. Protein misfolding during impaired proteostasis leads to aggregated or misfolded proteins, which can induce ER stress. Unfolded protein response (UPR), a signal transduction pathway, is activated in response to ER stress. Importantly, transmembrane ER-resident proteins including inositol requiring enzyme 1α (IRE1α), PKR-like ER kinase (PERK), and activating transcription factor 6α (ATF6α) are activated during UPR activation. UPR is primarily activated to increase adaptive response and restore protein folding, but prolonged ER stress causes adaptive response failure and activates terminal UPR signals promoting cellular apoptosis [2–4].

ER stress is extensively studied, but ER stress response failure and its cellular fate linked studied are limited. Previously, we proposed that the failure of the ER stress response could be associated with several metabolic diseases including aging [4,5]. Aging is a very complex process and cannot be explained by a single mechanism. The ER chaperones and foldases are generally impaired during aging and lead to improper

* Corresponding author. Department of Dental Pharmacology, College of Dentistry, Jeonbuk National University, Jeonju, 54896, Republic of Korea.
** Corresponding author. School of Pharmacy and Institute of New Drug Development Jeonbuk National University, Jeonju, 54896, Republic of Korea.
E-mail addresses: hrkimdp@gmail.com (H.-R. Kim), hjchae@jbnu.ac.kr (H.-J. Chae).
[1] These authors contributes equally.

https://doi.org/10.1016/j.redox.2021.102128
Received 10 May 2021; Received in revised form 30 August 2021; Accepted 6 September 2021
Available online 9 September 2021

protein folding [6]. Additionally, imbalance in redox signaling or aberrant redox-associated post-translational modifications increases protein structure or functional altercation and develops pathological conditions. However, the clear mechanisms of age-associated redox imbalance, and ER proteostasis impairment and their role in disease progression are unknown. Nonalcoholic fatty liver disease (NAFLD) is one of the most prevalent liver diseases, strongly associated with hyperlipidemia. NAFLD is caused by various factors, including reactive oxygen species (ROS) [7], impaired autophagy [8,9], and ER stress [8]. It affects one-third of the global population [10], resulting in metabolic disturbances including obesity, dyslipidemia, and type II diabetes. If left untreated, NAFLD progresses to nonalcoholic-steatohepatitis (NASH), fibrosis, cirrhosis, and hepatocellular carcinoma (HCC) [11]. The prevalence of NAFLD is more than 25% globally, of which more than 31% is in the United States of America alone, and the number is rising [12,13].

Transmembrane B cell lymphoma 2-associated X protein inhibitor motif-containing 6 (TMBIM6)/Bax Inhibitor-1 (BI-1) is an evolutionary conserved anti-apoptotic ER protein, and its protective function was originally identified as an apoptosis suppressor in yeast cells induced by pro-apoptotic Bax protein [14,15]. This study investigates the role of TMBIM6 in the regulation of aging and its associated hepatic phenotypes under normal diet conditions in mice and humans. Here, we identified the accumulation of excessive reactive nitrogen species (RNS) and reactive oxygen species (ROS) inducing nitro-oxidative stress, inciting oxidative modifications of cysteine during aging. This paradigm increased the modification of IRE1α, an ER membrane protein. S-nitrosylation and sulfonation of IRE1α altered the functioning of IRE1α. Our study uncovered the TMBIM6 regulation mechanism of aging-associated instability of the ER function and gave an insight into the molecular target of extending health span.

2. Materials and methods

2.1. Chemicals and reagents

GSNO (487920, Sigma-Calbiochem), HPDP Biotin (21341, Thermo Scientific), D-galactose (G0750, Sigma), Tunicamycin (CAS 11089-65-9, Calbiochem), and thapsigargin (CAS 67526-95-8, Calbiochem).

2.2. Plasmid

IRE1α plasmid was kindly donated by Yong Liu (University of the Chinese Academy of Sciences, China). C931S constructs of IRE1α were generated using Muta-Direct™ Site-directed Mutagenesis Kit (iNtRON Biotechnology, Republic of Korea) according to the manufacturer's instructions and confirmed by DNA sequencing. Plasmid expressing miR-338 was constructed by inserting synthesized human miR-338 sequence into pBIC-A vector (Bioneer, Republic of Korea).

2.3. Antibodies used for Western blot

Following primary antibodies were used unless specified. Alpha-SMA (sc-53142, anti-mouse, Santa-Cruz Biotechnology, Dallas TX, USA), Beta actin (sc-47778, anti-mouse, Santa-Cruz Biotechnology), Caspase 7 (9492S, anti-rabbit, Cell signaling), Caspase 12 (GTX132298, anti-rabbit, Genetex, CA, USA), GRP78 (sc-376768, anti-mouse), Santa-Cruz Biotechnology), p-eIF2α (3597S, anti-rabbit, Cell signaling), eIF2α (9722S, anti-rabbit, Cell Signaling), CHOP (2895S, anti-mouse, Cell signaling), ATF6α (sc-22799, anti-rabbit, Santa-Cruz Biotechnology), p-PERK (sc-32577, anti-rabbit, Santa-Cruz Biotechnology), PERK (sc-13073, anti-rabbit, Santa-Cruz Biotechnology), PDI (2446S, anti-rabbit, Cell signaling), PDI for HMWC (ADI-SPA-891-F, anti-mouse, Enzo Life Sciences, Inc., Farmingdale, NY, USA), p-IRE1α (ab48187 anti-rabbit, Abcam, Cambridge, UK), IRE1α (3294S, anti-rabbit, Cell signaling), sXBP-1 (sc-7160, anti-rabbit, Santa-Cruz Biotechnology), p-JNK (9251S, anti-rabbit, Cell Signaling), JNK (9252S, anti-rabbit, Cell Signaling), Bcl-2 (3498S, anti-rabbit, Cell signaling), anti-HA (11867423001, anti-rat, Roche), BCL-XL (2764S, anti-rabbit, Cell signaling), MCL-1 (94296S, anti-rabbit, Cell signaling), Ubiquitin (sc-166553, anti-mouse, Santa-Cruz Biotechnology), cysteine sulfenic acid (07–2139, anti-rabbit, Millipore), cysteine sulfonate (ab176487, anti-rabbit, Abcam). Following secondary antibodies were used in this study. Anti-rabbit (1:10000, Jackson ImmunoResearch Laboratories, Inc.111-036-003), anti-mouse (1:10000, Jackson, 115-035-003), and anti-rat (1:5000, Jackson, 112-035-003).

2.4. Antibodies used for immunohistochemistry and immunofluorescence

TMBIM6 (MA1-41108, anti-mouse, Invitrogen), GRP78 (sc-376768, anti-mouse, Santa-Cruz Biotechnology, Dallas TX, USA), GADD153/CHOP (sc-575, anti-rabbit, Santa-Cruz Biotechnology), IRE1α (sc-390960, anti-mouse, Santa-Cruz Biotechnology), HA probe (sc-805, anti-rabbit, Santa-Cruz Biotechnology), cysteine sulfonate (ab176487, anti-rabbit, Abcam, Cambridge, UK), 4-HNE (ab46545, anti-rabbit, Abcam), 8-OHdG (ab48508, anti-mouse, Abcam), β-galactosidase (sc-377257, anti-mouse, Santa-Cruz Biotechnology), cleaved-caspase-3 (9664S, anti-rabbit, Cell signaling), and iNOS (ab3523, anti-rabbit, Abcam).

2.5. Human specimens

Randomly assigned seven young (20–30 years old) and fifteen aging (60–70 years old) human normal liver tissues adjacent to the tumor (NAT) were obtained from the Bio-Resource Center Biobank of Asan Medical Center, Seoul, Republic of Korea. Due to the challenges in collecting livers from normal healthy individuals, we used non-malignant normal liver tissue samples from hepatocellular carcinoma patients. Patient characteristics are shown in Supplementary Figure 8. Informed consent is obtained by Asan Medical Center and is available in its database. This study was approved by the Institutional Review Board (IRB) of Jeonbuk National University Hospital (IRB No: JBNU 2020-05-002-004). All relevant ethical guidelines were strictly followed during the study.

2.6. Human liver tissue microarray specimens

The liver tissue microarrays (TMA) were purchased from US Biomax (Derwood, MD, USA) and are IRB exempt. TMA for different diseases of the liver (LV1201a, 120 cores), liver cancer (BC03116a, 40 cores), and normal liver and HCC (LVN801, 80 cores) were purchased. This study includes 14 normal/15 fatty degenerates, 21 normal/9 fatty degenerates, and 42 normal/28 NAT for analysis. We also classified normal and degenerated fatty tissue of young (<50 years) and old patients (>50 years) from the same tissue array samples. All tumor cores from the tissue array were excluded from our study.

2.7. Animals and experimental design

Female C57BL/6 wild type (WT) and TMBIM6 knockout ($TMBIM6^{-/-}$) mice (n = 6–7/group), young (3–4 months), middle-aged (11–12 months), and old-aged (18–24 months) were used in this study. Female mice were selected based upon previous studies, which suggests that obesity is more prevalent in women than men of the same age group [16,17]. $TMBIM6^{-/-}$ mice were generated as described in our previous article [25]. Mice were housed at 22 ± 2 °C, 55%–60% relative humidity, and a 12-h light-dark cycle and maintained in specific pathogen-free housing conditions before their use in the experiments. Tap water and a standard pellet diet (NCD, normal chow diet) were provided ad-libitum throughout the experimental period. All the animal care and the experiments were conducted as per the regulations of the institutional guidelines of Jeonbuk National University, Jeonju, Republic of Korea (IACUC No: 2019-021, CBNU 2020-088).

2.8. Animal sacrifice

Mice were anesthetized intraperitoneally with a cocktail of ketamine and xylazine. Blood samples were collected from the abdominal aorta and placed in VACUETTE® Z Serum Clot Activator tubes. To collect serum, tubes were then centrifuged for 10 min at 2500 rpm, and the supernatant was transferred to a 1.5 mL Eppendorf tube and stored at −80 °C until used. Excised liver tissues were washed with normal saline, weighed, and kept on ice. One lobe was placed in formalin (Formaldehyde 3.7%, Dana, Seoul, Republic of Korea) for histological analysis, and the remaining lobes were frozen immediately and stored at −80 °C for molecular study.

2.9. Adenovirus-mediated TMBIM6 gene delivery in vivo

Adeno-GFP and adeno-TMBIM6 were used to infect the TMBIM6$^{-/-}$ old mice via tail vein injection as described previously [11]. The adenoviral vector expressing TMBIM6 (Ad-TMBIM6) was generated by homologous recombination between adenovirus backbone vector pAD-Easy and linearized transfer vector pADTrack and followed the protocol as described previously [11,18]. For adenovirus-mediated gene delivery in vivo, TMBIM6 knockout old mice were infected via a single injection of purified 1.0×10^9 PFU (diluted in 0.1 mL saline) in a volume of 50 μL of Ad-GFP or Ad-TMBIM6 adenoviruses via the tail-vein. Mice were fed with a normal diet, monitored body weight every week, and sacrificed after 4 weeks of inoculation. Blood samples were collected for serum, and livers were kept in formalin or optimal cutting temperature (OCT) compound for histological analyses and snap-frozen in liquid nitrogen and stored at −80 °C until used.

2.10. Cell culture and treatment

Human Hep3B and HepG2 cells were purchased from Korean Cell Line Bank (Seoul, Republic of Korea). Cells were cultured in Dulbecco's modified Eagle's medium (DMEM, WELGENE, Gyeongsan-si, Republic of Korea, Cat: LM-001-05), supplemented with 10% FBS, 100 μg/mL streptomycin, and 100 units/ml penicillin. Both cell lines were stably transfected with the pcDNA3 (EV: empty vector) and HA-pcDNA3-TMBIM6 plasmids as described previously [19] and used throughout the study. D-galactose was treated at 100 mM for 48 h. Palmitate at a concentration of 250 μM was treated for 12 h. Tunicamycin was treated at 5 μg/mL for 12 h.

2.11. RNA sequencing

RNA-seq analyses of mouse liver tissues were performed by Ebiogen (Seoul, Republic of Korea). Total RNA was isolated using Trizol reagent (Invitrogen). RNA quality was assessed by Agilent 2100 bioanalyzer using the RNA 6000 Nano Chip (Agilent Technologies, Amstelveen, The Netherlands), and RNA quantification was performed using ND-2000 Spectrophotometer (Thermo Inc., DE, USA). For control and test RNAs, the construction of library was done using QuantSeq 3′ mRNA-Seq Library Prep Kit (Lexogen, Inc., Austria) according to the manufacturer's instructions. The RC (Read Count) data were processed based on the quantile normalization method using EdgeR within R (R Development Core Team, 2016) using Bioconductor (Gentleman et al., 2004). Gene classification was based on searches done by DAVID (http://david.abcc.ncifcrf.gov/), Medline databases (http://www.ncbi.nlm.nih.gov/), Enrichr (https://maayanlab.cloud/Enrichr/) and Gene Set Enrichment Analysis (https://www.gsea-msigdb.org/gsea/).

2.12. In vitro IRE1α-mediated miR-338 and RNA cleavage assay

In vitro cleavage of miR-338 was performed as described previously with modifications [20]. In brief, pBIC-miR338 plasmids were linearized with *Xho*I containing T7 promoter region. After recovering ultrapure DNA using AccuPrep® PCR/Gel DNA Purification Kit (Bioneer, Daejeon, Republic of Korea), transcription of miR-338 was performed using the T7 RiboMax Express RNA Production System (Promega). In vitro-transcribed RNA (5 μg) was incubated with or without recombinant human IRE1α protein (IRE1c, SignalChem) or ATP (2 mmol/L final concentration) in cleavage assay buffer (20 mM HEPES, pH 7.0, 70 mM NaCl, 2 mM ADP, 2 mM $MgCl_2$, 5 mM DTT, 5% glycerol). The reaction products were resolved on 1.2% denaturing agarose gels after incubation at 37 °C for 30 min. In vitro TMBIM6 cleavage assay was performed as described previously [21]. 5′-Carboxyfluorescein (5-FAM)- and 3′-Black Hole Quencher (BHQ-3)-labeled single stem-loop minisubstrate for XBP1 (5′FAM-GAACAAGAUAUCCGCAGCAUAUACAGUUC-3′BHQ) and TMBIM6 (5′FAM-GAAGUGGGACCAGCAGAGGGCGCCAACUUC-3′BHQ), and SPARC (5′FAM-GUGGGAGAGAUCCCUGCAGAACCCAC-3′BHQ) were purchased from Bioneer. IRE1c was incubated with 50 μM RNA substrate for 20 min at 30 °C. The cleavage products were quenched by adding urea to a final concentration of 4 M and resolved by 19% urea-PAGE.

2.13. Nuclear fractions

Total 50 mg of liver tissue was washed with PBS, and added buffer containing 20 mM HEPES-KOH (pH 7.5), 10 mM KCl, 1.5 mM $MgCl_2$, 1 mM sodium EDTA, 1 mM sodium EGTA, 250 mM sucrose, 1 mM DTT, and 0.1 mM PMSF, and then kept in ice for 20–30 min. Tissue was homogenized using a Micro Tissue homogenizer. Tissue homogenates were centrifuged 2–3 times for 10 min at 1000 g at 4 °C. The pure pellet was collected in an Eppendorf tube as a nuclear fraction and frozen at −80 °C. The pellets were resuspended in RIPA buffer and processed for the Western blot.

2.14. Lipid peroxidation measurement

Lipid peroxidation was detected in liver tissue homogenates using OxiSelect™ TBARS Assay Kit (STA-330, Cell Biolabs, Inc. San Diego, CA, USA). Briefly, MDA standards or samples were mixed with SDS lysis solution and incubated at room temperature (RT) for 5 min. Both MDA standards and samples were then reacted with thiobarbituric acid (TBA) reagent at 95 °C for 45–60 min. Tubes were then cooled in an ice bath for 5 min and centrifuged the sample and standard tubes at 3000 rpm for 15 min. The supernatant was collected and measured spectrophotometrically at 532 nm.

2.15. Detection of high molecular weight complex

Whole liver homogenates were used to detect the high molecular weight complexes (HMWC) of PDI in different age groups of WT and TMBIM6$^{-/-}$ mice. Briefly, liver tissue was washed twice with ice-cold PBS supplemented with 1 mM PMSF, lysed in lysis buffer (150 mM NaCl; 1% Triton X-100; 50 mM Tris-HCl; pH 7.5) for 30 min on ice. The tissue was homogenized, sonicated, and cleared by centrifugation (13000 rpm, 30 min, and 4 °C). The total protein concentration of lysates was measured by Bio-Rad protein assay (Bio-Rad, Hercules, CA, USA). 30 μg of total protein was separated on non-reducing conditions (no SDS, no mercaptoethanol, and no boiling) using 8% polyacrylamide gels and run at 75 V at 4 °C to detect the high molecular weight complex of PDI.

2.16. In situ proximity ligation assay (PLA)

Duolink PLA was performed to detect the interactions between two proteins in the hepatic cells and tissues. The PLA signals or the interaction between proteins were identified by the red dots. The assay was performed using the Duolink PLA fluorescence kit protocol (Sigma-Aldrich, St. Louis, MO, USA). Briefly, the cells were washed with PBS, fixed with methanol, and again washed with PBS. The formalin-fixed

paraffin-embedded liver sections (5 μm) were deparaffinized and rehydrated following the antigen retrieval. Cells and tissue sections slides were applied with blocking solution (60 min/37 °C) and incubated with primary antibodies (anti-mouse IRE1 1:100, anti-rabbit HA, Santa Cruz 1:100), and (anti-mouse IRE1 1:100, anti-rabbit cysteine sulfonate, Abcam 1:100) in a humidity chamber overnight at 4 °C. The slides were followed by hybridization of PLA probes (1 h/37 °C), ligation (30 min/37 °C), and amplification (2 h/37 °C). The concentration of the reagents is described in the manufacturer's protocol. The cells and tissues were washed appropriately following the manufacturer's instruction and were mounted with aqueous in situ DAPI and analyzed using a confocal microscope using at least 40× objectives. The red dots were observed to be PLA positive signals.

2.17. Detection of S-nitrosylation

General S-nitrosylation was detected in liver homogenates using a commercial Pierce S-nitrosylation kit provided by Thermo Scientific (#90105), which enables detection of protein S-nitrosocysteine post-translational modifications (PTMs). The test was done according to the manufacturer's instructions. Briefly, S-nitrosylated proteins were reacted with MMTS to block free sulfhydryls. S-nitrosocysteines were selectively reduced with ascorbic acid for labeling with the iodoTMT reagents. Western blot was performed to detect the TMT-labeled proteins using an anti-TMT antibody.

2.18. Biotin-switch assay

S-nitrosylation protein was analyzed in liver sections from young and old WT and TMBIM6$^{-/-}$ mice. In situ detection of S-nitrosylated protein was performed using a modified biotin switch method. Briefly, after deparaffinization and rehydration of the liver sections, the sections were washed with 1xPBS (3 times) containing 0.4 mM EDTA and 0.04 mM neocuproine. Free thiol groups were blocked with 20 mM MMTS (Pierce) in PBS containing 0.4 mM EDTA, 0.04 mM neocuproine, and 2.5% SDS for 30 min. The blocking solution was removed and washed with 1xPBS (3 times) (composition as in the first step). Sections were then incubated with 20 mM sodium ascorbate (in PBS) for 15 min to reduce S-nitrosylated proteins. No sodium ascorbate was added to the negative control sections. Newly reduced cysteine residues were then labeled with 0.25 mg/mL biotin-HPDP (in PBS) for 30 min. Excess biotin was removed by washing 3 times with 1XPBS (composition as in the first step). Sections were then incubated at 4 °C/overnight with a fluorophore-tagged streptavidin Alexa Fluor 568 and IRE1α antibody (sc-390960) conjugated to Alexa Fluor 488 to visualize biotinylated proteins, followed by washing 3 times with 1XPBS. Cell nuclei were counterstained with DAPI. Images were acquired using a confocal laser scanning microscope. The entire procedure was carefully performed under protection from direct light.

2.19. TUNEL assay

TUNEL (Terminal deoxynucleotidyl transferase UTP Nick-End Labeling) assay was performed to detect DNA fragmentation, an important hallmark of late-stage apoptosis. TUNEL assay was performed using in situ Cell Death Detection Kit, TMR Red (no. 12156792910; Roche, Indianapolis, IN). Briefly, the formalin-fixed, paraffin-embedded liver tissue was sectioned at 5 μm thickness. Sections were deparaffinized, rehydrated in a series of ethanol (100%, 95%, and 70%) until distilled water is used. Sections were treated with 10 μg/mL Proteinase K solution (Biosesang, Gyeonggi-do Seoul, Republic of Korea) and incubated for 20 min at RT. Slides were then rinsed with PBS two times at 5 min intervals. TUNEL reaction mixture (Enzyme solution and Label solution, ratio 1:9) was added to the sections and incubated at 37 °C for 60 min in a humidified atmosphere in the dark and rinsed 3 times in PBS for 5 min each. The slides were then mounted with DAPI (Molecular Probes, Eugene, OR) and observed by using confocal laser microscopy at 60× magnification. Red fluorescence (TUNEL positive) cells were detected using a TRITC channel and the nucleus was detected using a DAPI channel. Cells were counted in 3–5 high-power fields of each tissue section (n = 6) and calculated the TUNEL positive cells in percentage.

2.20. Lipid profile test

Serum cholesterol, serum ALT, serum AST, serum triglyceride, and hepatic triglyceride were measured according to the manufacturer's instruction by using the commercially available kits (Asan Bio, Seoul).

2.21. Hepatic lipid extraction for triglyceride measurement

Hepatic lipid was extracted using the slightly modified Bligh and Dyer method [22]. Briefly, the liver tissue (using ~50 mg) was pelleted, added the chloroform and methanol at a ratio of 1:2. Vortexed for 15 min and added the chloroform and distilled water (50 μL each). It was then centrifuged at 3000 rpm for 5 min at RT to give a two-phase system (aqueous top, organic bottom). Recovered the bottom phase as follows: Insert Pasteur pipette through the upper phase with gentle positive pressure (i.e., gentle bubbling) so that the upper phase does not get into the pipette tip. When the pipette tip is at the bottom of the tube, carefully withdraw the bottom phase through the pipette, making sure to avoid the interface or upper face (should only try to recover ~90% of the bottom phase, not all of it). Evaporate by heating at 55 °C and add 50–100 μL of RIPA buffer (extraction buffer). Suspend it at 37 °C overnight. It was then spun and measured spectrophotometrically using the commercially available kit (Asan Bio, Seoul, South Korea).

2.22. Morphological staining (H&E)

Formalin-fixed hepatic tissue was routinely processed and embedded in paraffin wax. The liver sections were cut at 5 μm thickness using a rotary microtome (Leica). Sections were then rehydrated and processed staining with Mayer's hematoxylin and 1% eosin. Sections were dehydrated and cleared with 2 changes of xylene. Mounting was done by using anhydrous media (Merck, Darmstadt, Germany), dried, and observed in a light microscope.

2.23. Sirius Red stain

Formalin-fixed, paraffin-embedded liver sections were sectioned at 5 μm thickness. The slides were then incubated and stained with a 0.1% Sirius Red solution by following the previous protocol [23]. The red color in the figure (green arrows) indicates the presence of collagen and fibrotic area. The red color in the figure (green arrows) indicates the presence of collagen and fibrotic area.

2.24. Oil Red 'O' staining

Formalin-fixed mouse liver tissue was gently wiped with tissue paper and submerged the tissue in 20% and 30% sucrose solution (prepared in PBS). The tissue specimen was embedded in an OCT compound (Leica Biosystems, Buffalo Grove, IL, USA) for cryosectioning. Human liver tissue was embedded directly in an OCT compound. The tissue was cut at 8 μm thickness using cryo-microtome. Cryosections were placed in cold formalin for 5 min, 60% isopropanol for 3 min, and stained with 0.3% Oil Red O solution in isopropanol for 20 min. The slides were washed with 60% isopropanol for 5 min, rinsed with tap water for 5 min, and processed for hematoxylin counterstaining. Slides were then washed with tap water for 5 min and mounted in an aqueous medium. Images were captured using an Eclipse TE2000 inverted microscope (Nikon, Melville, NY, USA) at 40× magnification.

2.25. DHE and DHR-123 stain

Dihydroethidium (DHE) and Dihydoxy-rhodamine-123 (DHR-123) were used to evaluate intracellular ROS and peroxynitrite production, respectively in tissues and human cell lines. Fixed tissues and cells were exposed to DHE (ThermoFisher Scientific, MA, USA) and DHR-123 (Invitrogen, Carlsbad, CA, USA) at a concentration of 10 and 20 μM respectively for 30 min/37 °C, followed by washing with PBS (x3), stained with DAPI and images were captured using confocal microscopy. Relative fluorescence intensity was analyzed with ImageJ (National Institutes of Health, Bethesda, MD, USA).

2.26. Immunohistochemistry and immunofluorescence

Paraffin-embedded TMA sections were purchased from US Biomax. The formalin-fixed, paraffin-embedded human and mouse liver tissue sections were sliced at 5 μm thickness and processed as described previously [24]. Similarly, immunofluorescence was performed as described earlier [24]. Images were obtained by confocal laser scanning microscope LSM 880 (Carl Zeiss, Germany) installed at the Center for University-Wide Research Facilities (CURF), Jeonbuk National University. ImageJ was used for analyzing of data. The results were expressed as a percentage of area stained that corresponds to the level of protein.

2.27. Immunoblotting

Immunoblotting was performed using whole liver homogenates by following the previous protocol [24]. Antibodies used in immunoblotting are described above. Optical densities of the bands were measured with ImageJ, and results were expressed in relative intensity from 3 to 6 independent experiments.

2.28. Detection of senescent cells

Hep3B and HepG2 cells having vector or expressing TMBIM6 were cultured and treated with different chemicals (as described above). Cells were then stained for endogenous β-galactosidase using senescence β-galactosidase staining kit (Cell Signaling, #9860) and CellEvent Senescence Green probe kit (ThermoFisher Scientific, C10850) per the manufacturer's instruction. Green color indicating β-gal or senescence positive cells were visualized under light microscope. The images were analyzed with ImageJ, and results were expressed in relative intensity from 3 to 5 independent experiments.

2.29. Quantitative real-time polymerase chain reaction (qRT-PCR)

The mRNA expression level was determined by quantitative real-time PCR as described previously [25]. Briefly, total RNA was isolated from liver tissue using Trizol reagent (Invitrogen Life Technologies, CA, USA) and complementary DNA (cDNA) was synthesized using a SuperScript™ III First-Strand Synthesis System (Invitrogen) following the manufacturer's protocols. PCR was performed using SYBR Green PCR Master Mix (Applied Biosystems, CA, USA). The reaction conditions using a PE Biosystems ABI PRISM 7700 Sequence Detection System were as follows: initial denaturation at 95 °C for 5 min, followed by 40 cycles at 94 °C for 10 s, 51–55 °C for 10 s, and 72 °C for 30 s. The relative mRNA expression was calculated using the $2^{-\Delta\Delta Ct}$ method and normalized to actin mRNA expression.

For spliced XBP1 and CYP2E1, we used TaqMan gene expression assay and followed the protocol as described in our previous paper [25]. The murine and human primer sequences used in this study are listed in Supplementary Tables S1 and S2, respectively. The PCR condition used for the test as follows: 50 °C -2'; 95 °C −10'; (95 °C −15''; 60 °C -1′)-40 cycles.

2.30. Bioinformatics and statistics

STRING version 11.0 was used for predicting protein-protein interactions. Parameters used for constructing interaction networks are described in figure legend of Supplementary Fig. 1. All statistical analyses were performed and plotted using GraphPad Prism 9.0. software (GraphPad Software, Inc., San Diego, CA). Data were presented as mean ± SEM. Differences in means were analyzed using the unpaired Student's t-test (for comparison between two groups). One-way and two-way analysis of variance (ANOVA) followed by Tukey's test was used to compare multiple groups. A p-value of * 0.05, ** 0.01, *** 0.001, **** 0.0001 was set as the criterion for statistical significance between groups. In each case, the statistical test used and the number of experiments is given in each figure legend.

3. Results

3.1. TMBIM6 is downregulated in fatty degeneration, and in aged human and mice liver

Expression profiles were analyzed by hierarchical clustering in young and old samples to understand the effect of aging on various functional gene sets (Fig. 1A). Among several genes, the expression of the TMBIM6 gene was markedly decreased in old mice liver. Gene ontology (GO) pathway analysis with Enrichr was carried out for up/down-regulated differentially expressed genes (DEGs). Biological process enrichment suggests that down-regulated DEGs were significantly enriched in the cellular response to ATP, activation of MAPKKK activity, PERK-mediated UPR, and ER stress-induced intrinsic apoptotic signaling pathway. Protein maturation, cyclic-nucleotide-mediated signaling, and protein processing GO were significantly enriched as up-regulated DEGs (Fig. 1B).

To investigate the role of TMBIM6 in hepatic lipid accumulation, we first analyzed TMBIM6 protein and mRNA expression in various human and mice liver samples in different conditions such as age-dependent, normal, and degenerative fatty tissues. We observed that the expression of TMBIM6 was significantly lower in fatty degenerative liver tissues than the normal liver tissues (Fig. 1C and D), with no differences in normal liver tissue and histological NAT (Fig. S1A). Similarly, fatty tissues from old patients had lower expression of TMBIM6 than younger counterparts (Fig. 1E). Next, we observed reduced TMBIM6 expressions in the old mice liver than younger counterparts (Fig. 1F and G). The STRING database clearly suggests that TMBIM6 is associated with the ER stress sensors, specifically to IRE1α/ERN1 and ATF6α (Figs. 1H, S1B, S1C), and apoptosis (Fig. S1D). These protein-protein interactions indicate that TMBIM6 regulates ER stress and ER stress-mediated apoptosis.

3.2 TMBIM6 knockout induces senescence, nitro-oxidative stress and hepatic steatosis during the aging process

To assess the impact of TMBIM6 deficiency on the development of obesity, we used WT and TMBIM6 knock-out mice and divided them into different age groups (Fig. 2A). It was interesting to note that aging-induced obesity was more pronounced in TMBIM6$^{-/-}$ mice, and these mice had gained central adiposity and body size (Fig. S2A), body weight (Fig. S2B), and liver weight (Fig. S2C) than WT mice of the same group. Total cholesterol level was higher in TMBIM6$^{-/-}$old mice than WT old mice (Fig. S2D). Serum and hepatic triglyceride levels were found to be increased in TMBIM6$^{-/-}$ old mice compared to younger and WT counterparts (Figs. S2E and S2F). In RNA-seq data, biological process enrichment suggests that upregulated DEGs were significantly enriched in fatty acid metabolic process, lipid metabolic process, and acetyl-CoA metabolic process in old-aged Tmbim6$^{-/-}$ mice liver (Fig. 2B and C). A recent study suggested that cellular senescence drives age-dependent hepatic steatosis [26]; therefore, we investigated whether TMBIM6$^{-/-}$

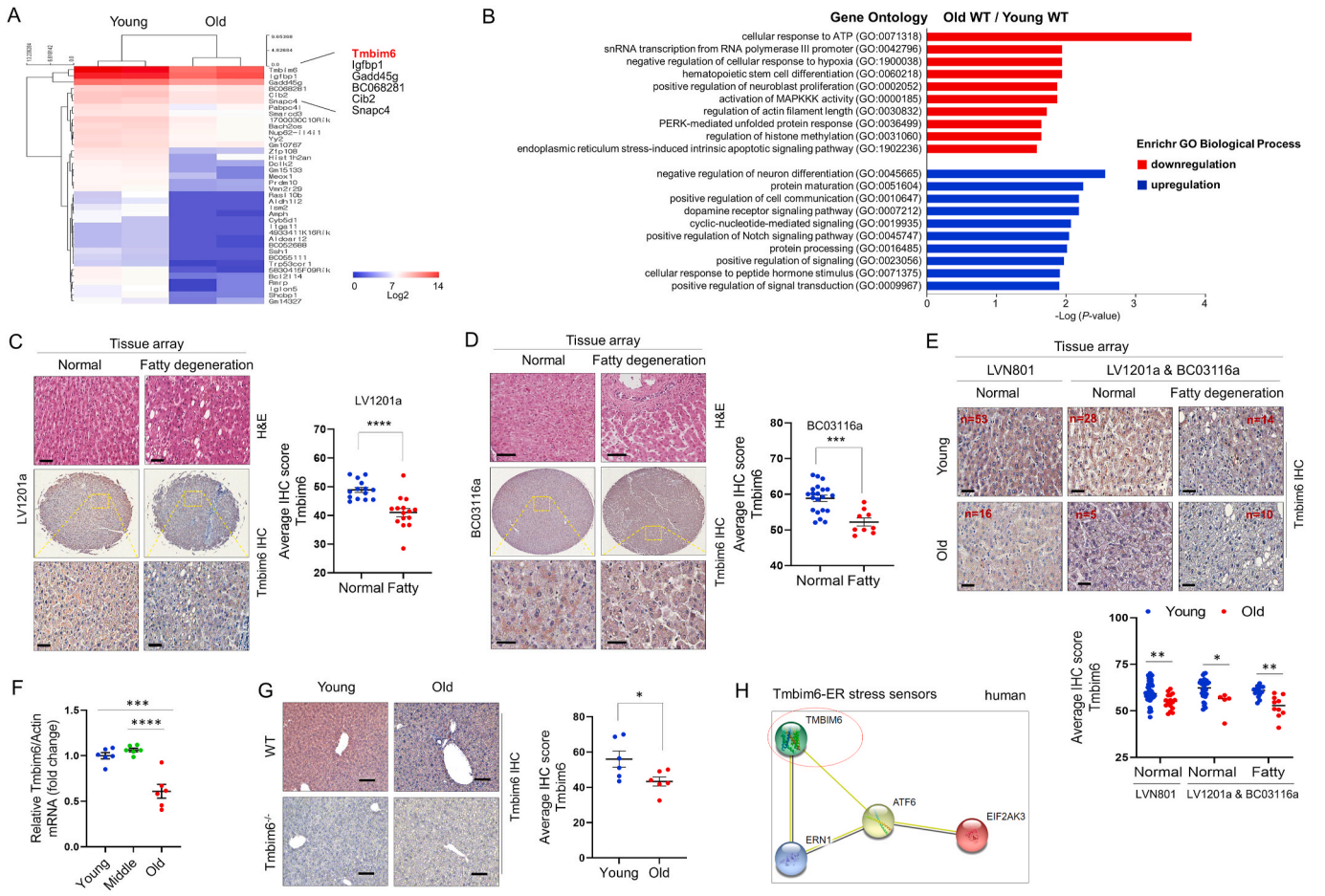

Fig. 1. TMBIM6 is downregulated in fatty degenerated and in aged human and mice livers. The liver was isolated from young and old WT mice and subjected to RNA-sequencing. (A) Hierarchical clustering of genes expressed in young and old WT mice. (B) Enrichment analysis results of up/down-regulated differentially expressed genes (DEGs) in old-aged mice compared to young mice. (C–D) Human normal and fat-degenerated liver sections were selected from tissue microarray (LV1201a and BC03116a) and analyzed for H&E and immunohistochemistry using TMBIM6 antibody. H&E images were adopted from Biomax. The bar graph (right) shows the average TMBIM6 expression score (LV1201a: normal = 14, fatty = 15; BC03116a: normal = 21, fatty = 9). Scale bar: 50 μm. (E) Normal tissues and fat-degenerated tissues were selected from young (<50 years) and old patients (>50 years) (selected as explained in the method section), and TMBIM6 expression was analyzed by immunohistochemistry using a specific antibody. Bar graph (below) shows the average TMBIM6 expression (total young normal = 81, total old normal = 21, young fatty = 14, and old fatty = 10). Scale bar: 50 μm. (F) TMBIM6 mRNA expression was analyzed by real-time PCR in different age groups of wild-type mice. (G) Immunohistochemistry of the expression of TMBIM6 in liver sections of young and old WT and TMBIM6$^{-/-}$ mice. The graph (right) shows the average TMBIM6 expression score (n = 6 per group). Note: TMBIM6$^{-/-}$ mice liver sections were used to validate the antibody and expressed none. Scale bar: 100 μm. (H) TMBIM6 association with various proteins of ER stress sensors (human ERN1/IRE1, EIF2AK3/PERK, and ATF6). The figure was plotted using STRING, a functional protein association network. The detail is in the legends of Supplementary Fig. 1. All the data are represented as mean ± S.E.M. *p < 0.05, **p < 0.01, ***p < 0.001, ****p < 0.0001 indicate significant differences indicated as specified in the bar graph.

old mice develop senescence or not. Interestingly, senescent cells were more prominent in TMBIM6$^{-/-}$ middle-age and old-age mice ($p < 0.0001$) than WT counterparts (Fig. 2D). Histological analysis revealed that the liver from TMBIM6$^{-/-}$ old mice accumulated high-lipid droplets (Figs. S2G and S2H) and developed mild fibrosis (Figs. S2I and S2J) than WT groups, indicating that TMBIM6 deficiency causes hepatic fat accumulation and an increase in senescent cells at least during the aging process.

The free radical theory of aging (FRTA) has long been the recognized aging theory. The continuous accumulation of damaged DNA or proteins arising from adduct formation with lipid peroxidation products is one of the concepts in this theory [27]. Therefore, we analyzed the lipid peroxidation, 8-hydroxy-2′-deoxyguanosine and 4-hydroxynonenal expression as oxidative stress markers and found that their levels were significantly higher in TMBIM6$^{-/-}$ old mice liver than WT old mice (Figs. S3A–S3C). We performed DHE (an indicator of ROS) and DHR-123 (an indicator of RNS) fluorescence staining to identify the involvement of free-radical mediated oxidative or nitrosative stress. Observations show a higher level of ROS and RNS in TMBIM6$^{-/-}$ middle-age and old-age mice liver samples than WT mice (Fig. 2E and F). Furthermore, our results demonstrated that the TUNEL-positive cells and cleaved caspases 12, 7, and 3 were significantly higher in TMBIM6$^{-/-}$ middle and old-age mice than their WT counterparts where WT and TMBIM6$^{-/-}$ young mice did not exhibit visible differences in apoptotic cells (Figs. S3D, 2G, 2H). These findings collectively suggest TMBIM6 as a cytoprotective protein against aging-associated oxidative stress and hepatic cell death.

3.3. Loss of TMBIM6 enhances impaired ER stress response and proteostasis during aging

We hypothesized that the level of ER chaperone protein like BiP/GRP78 decline and proteins involved in ER stress-mediated apoptotic signaling are increased with age. Thus, we aimed to determine the expression of the UPR elements in the liver of young and old mice. We found that the old mice displayed much lower GRP78 and p-eIF2α while

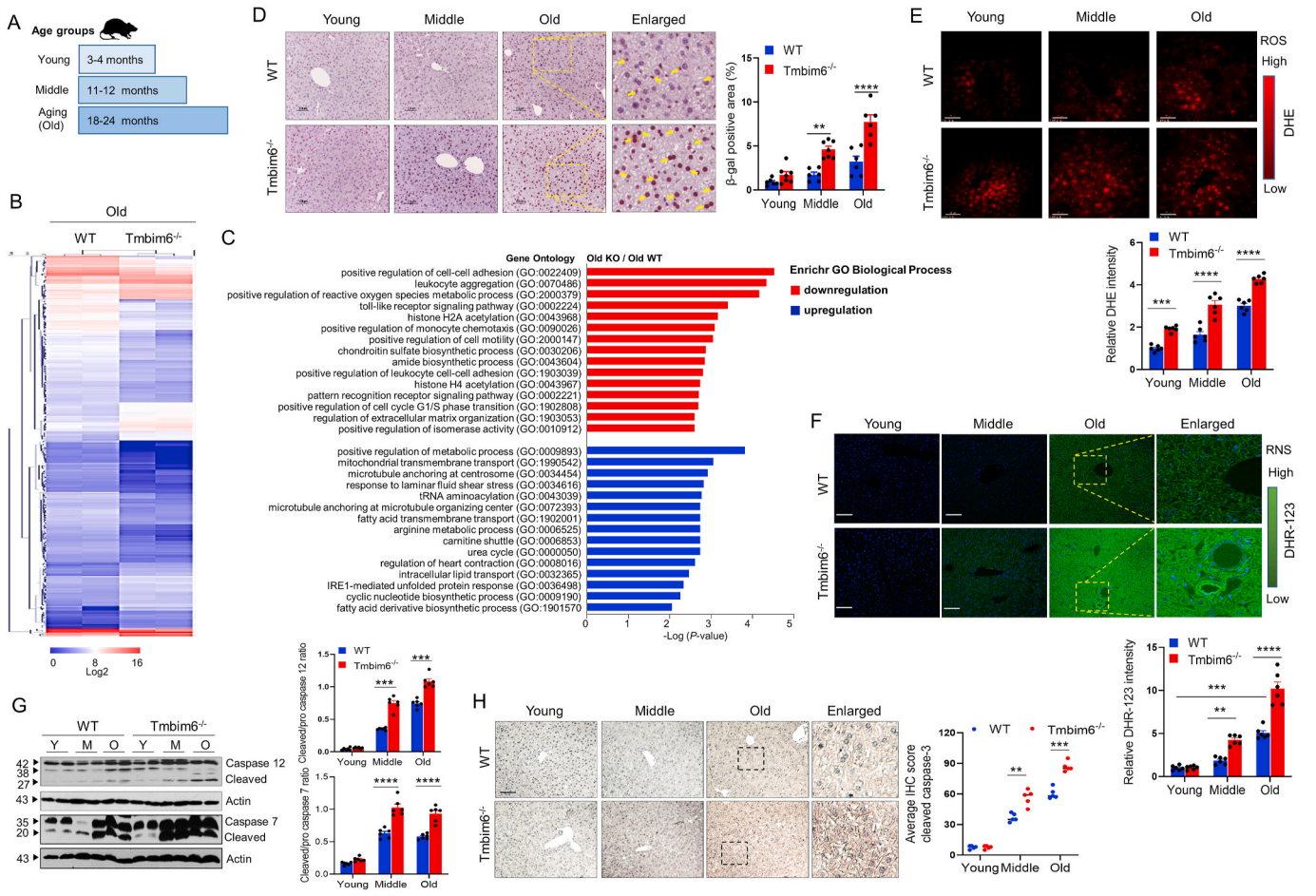

Fig. 2. TMBIM6 knockout induces senescence, nitro-oxidative stress and apoptosis during the aging process. (A) Animal groups and model of the study. (B) Hierarchical clustering of genes expressed in old WT and TMBIM6$^{-/-}$ mice. (C) Enrichment analysis results of up-and down-regulated differentially expressed genes in old-aged Tmbim6$^{-/-}$ mice compared to old-aged WT mice. (D) Representative immunohistochemistry images indicating the expression of β-galactosidase of the indicated groups. The graph on the right is the measurement of β-galactosidase positive staining. Yellow arrows indicate the predominant nuclear expression of β-galactosidase. Scale bar: 100 μm. (E–F) ROS and RNS generation was assessed by fluorescent microscopy using DHE (10 μM) and DHR-123 (20 μM) staining in the liver sections of the indicated groups and genotypes. The bar graph (below) shows the relative fluorescence intensity to young WT (n = 6 per group). Scale bar: 25 μm. (G–H) Western blots showing the expression of caspase 12 and 7 (G) and immunohistochemistry of the cleaved caspase 3 (H) in the liver of WT and TMBIM6$^{-/-}$ mice of the indicated groups. The relative intensities are shown in graph (right) (n = 6 per group). Y: Young, M: Middle, O: Old age. All the data are represented as mean ± S.E.M. *p < 0.05, **p < 0.01, ***p < 0.001, ****p < 0.0001 indicate significant differences indicated as specified in the bar graph. (For interpretation of the references to color in this figure legend, the reader is referred to the Web version of this article.)

proteins involved in cell death (p-JNK and CHOP) were upregulated (Fig. 3A). These data demonstrate that all ER stress response elements are not activated during aging, indicating impaired ER stress signaling that follows the apoptotic process in the aging liver.

Since TMBIM6 expression was reduced in the aging liver (Fig. 1F and G), we examined the protein expression levels of different UPR elements in WT and TMBIM6$^{-/-}$ mice liver of different age groups. Aging-associated loss of GRP78 was significantly enhanced in middle-age and old-age TMBIM6$^{-/-}$ mice than old WT mice (Figs. 3B, S4A), which suggests a reduction in the chaperone function in TMBIM6$^{-/-}$ mice during the aging. Furthermore, we verified the total expression and nuclear translocation of CHOP, a strong marker of ER stress-mediated apoptosis, and found that the CHOP expression was highly increased in the old mice and was further elevated in TMBIM6$^{-/-}$ old mice (Figs. 3B, 3C, S4B). WT old mice showed reduced p-eIF2α with no significant changes in ATF6α and p-PERK, but in TMBIM6$^{-/-}$ mice, these components were reduced in middle and old age conditions (Figs. 3B, S4C). Surprisingly, we observed increased expression of ATF4, p-IRE1α and its downstream JNK in the old TMBIM6$^{-/-}$ mice liver than old WT mice. However, sXBP1 (critical for cell survival) was not activated, indicating the impaired ER stress response from the IRE1α sensor in old TMBIM6$^{-/-}$ mice (Fig. 3B). Moreover, the expression of the anti-apoptotic BCL-2, BCL-XL, and MCL-1 were downregulated significantly in TMBIM6$^{-/-}$ old mice triggering enhanced cell death signals. No apparent differences were observed in all the groups of WT mice (Fig. S4C).

To better understand the IRE1α sensor response, the expression of sXBP1 was assessed using quantitative real-time PCR and found that sXBP1 was significantly increased in old WT mice, but not in old TMBIM6$^{-/-}$ mice (Fig. 3D) regardless of IRE1α activation, indicating an ER stress response failure in old TMBIM6$^{-/-}$ mice. We further assessed sXBP1 expression in the hepatic nuclear fractions and found that sXBP1 was intact in young groups, but unexpectedly it was lower in old TMBIM6$^{-/-}$ mice than WT mice, suggesting a defective sXBP1 nuclear translocation in old TMBIM6$^{-/-}$ mice (Fig. 3E). Furthermore, sXBP1 target genes such as Edem1, Erdj4 (also involved in ERAD function), and PDI were attenuated in TMBIM6$^{-/-}$ mice (Fig. 3F, S4C), suggesting reduced degradation capacities and failure to maintain ER quality control during aging. Regulated IRE1α-dependent decay (RIDD), which degrades a subset of endogenous mRNA, was also confirmed by PCR. RIDD target genes such as CYP2E1, HGSNAT, and COL6 mRNA were decreased in TMBIM6$^{-/-}$ old mice compared to WT old mice (Fig. 3G).

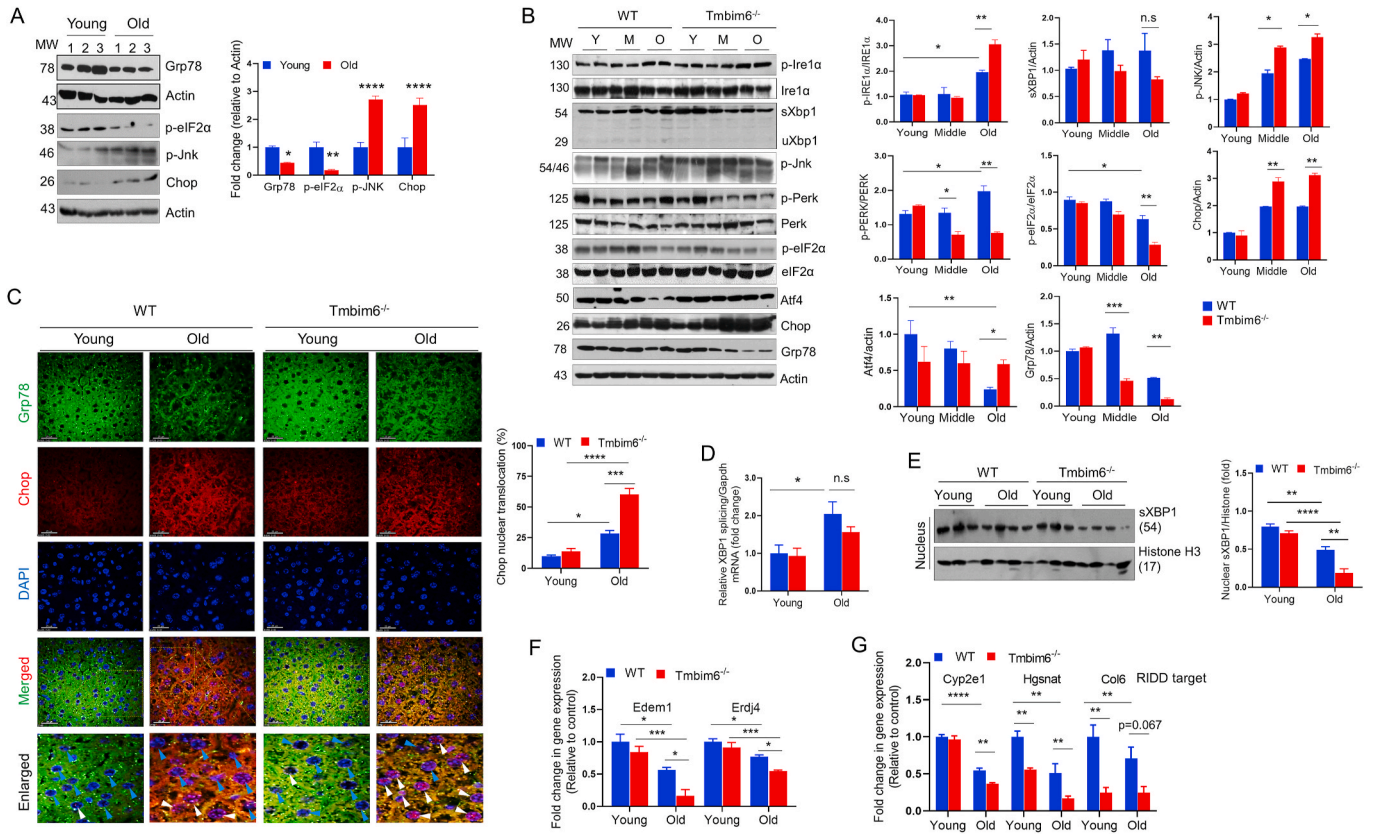

Fig. 3. Loss of TMBIM6 enhances impaired ER stress response during aging. (A) Immunoblot analysis of indicated proteins in young and aged liver. The bar graph (right) shows the relative band intensity of the indicated proteins (n = 6 per group). (B) The expression of several UPR elements/ER stress marker proteins in the liver of WT and TMBIM6$^{-/-}$ mice of different age groups. Bar graphs (right) show the band intensity of the indicated proteins to their loading control (n = 4 per group). Y: Young, M: Middle, O: Old age. (C) Representative confocal laser immunofluorescence photomicrography showing expressions of GRP78 (ER marker, green fluorescence) and CHOP (expressed in both cytoplasm and nucleus, red fluorescence) in the WT and TMBIM6$^{-/-}$ mice of indicated age groups. DAPI stain was used for nuclear localization. Red, green, and blue images were acquired using TRITC, FITC, and DAPI channels of the confocal microscope. The lowest panels show the merger views. Blue triangles indicate CHOP expression having no nuclear *trans*-localization and white triangles indicate the CHOP nuclear *trans*-localization. Magnification: 60×, Scale bar: 25 μm. TRITC, tetramethylrhodamine isothiocyanate; FITC, fluorescein isothiocyanate; DAPI, 4′, 6-diamidino-2-phenylindole. The bar graph (below) shows the percentage of CHOP nuclear *trans*-localization of the indicated groups. (D) sXBP1 mRNA was analyzed by real-time PCR and a graph was plotted to the ratio with Gapdh (normalization). (E) The expression of sXBP1 was shown at the nuclear level from the liver of WT and TMBIM6$^{-/-}$ young and old mice (n = 3–4 per group). Histone was used as a nuclear marker. The intensity of the sXBP1 expression is shown in the bar graph (right). (F) The mRNA expression of XBP1 target genes such as Edem1 and Erdj4 were analyzed by real-time PCR and the graph was plotted to the ratio with Gapdh. (G) The mRNA expression of RIDD substrates such as Cyp2e1, Hgsnat, and Col6 was analyzed by real-time PCR and the graph was plotted to the ratio with Gapdh (n = 6 per group). Gapdh was used as a loading control. All the data are represented as mean ± S.E.M. *p < 0.05, **p < 0.01, ***p < 0.001, ****p < 0.0001 indicate the significant differences among the groups. n.s; not significant. (For interpretation of the references to color in this figure legend, the reader is referred to the Web version of this article.)

The expression of PDI, an ER-resident foldase with ER folding capacity was examined and found to be significantly decreased in TMBIM6$^{-/-}$ aged liver (Fig. S4C). The accumulation of HMWC PDI was found to be higher in old TMBIM6$^{-/-}$ mice (Fig. S4D) which compromises protein folding and lead to the formation of insoluble multiprotein complexes, eventually alter the protein folding capacity and induce cellular apoptosis [28]. Furthermore, the total ubiquitin levels were also higher in old TMBIM6$^{-/-}$ mice, indicating that there may be a lot more damaged or unfolded proteins and were unable to eliminate misfolding proteins properly (Fig. S4E). Overall, these data suggest that with aging, protein folding capacity decline, and its demand disrupts ER homeostasis and triggers pro-apoptotic signaling. TMBIM6$^{-/-}$ mice showed severely impaired ER stress response and apoptosis, and in turn, exaggerated the hepatic steatosis during aging (Fig. S4F).

3.4. *TMBIM6 deficiency in aging increases redox-mediated post-translational modifications of IRE1α*

To understand how the loss of TMBIM6 reduces the splicing of XBP1 during aging, we hypothesized that redox-mediated PTM of proteins alters the function of IRE1α. It is known that additional PTMs of cysteine residues are influenced by S-nitrosylation (SNO) and inhibits the protein function (e.g., PDI) during severe nitrosative stress [29,30]. Other redox PTMs of thiols, such as sulfenylation (SOH) or sulfonation (SO_3H), can alter protein function by modifying protein structure or altering interactions with other proteins. Depending on the degree of oxidation, redox PTMs are classified as reversible and irreversible [31]. Since RNS and ROS-mediated nitro-oxidative stress was highly increased in TMBIM6$^{-/-}$ mice, we tried to detect the RNS and ROS-influenced cysteine modifications such as SNO, SOH, and SO_3H in TMBIM6$^{-/-}$ mice. SNO, SOH and SO_3H levels of general proteins were greatly accumulated in TMBIM6$^{-/-}$ aging liver than WT mice liver (Figs. S5A–S5C). Therefore, we examined the SNO and SO_3H of IRE1α to differentiate whether they can affect the ER function in young and old liver tissues of WT and TMBIM6$^{-/-}$ mice. WT old mice exhibited a high level of SNO-IRE1α than its young mice; however, SNO-IRE1α was significantly increased in TMBIM6$^{-/-}$ old mice than WT mice (Fig. 4A). Similarly, PLA data (red dots, PLA positive) suggest that the interaction between IRE1α and SO_3H was highly pronounced in old TMBIM6$^{-/-}$ mice than WT old mice (Fig. 4B).

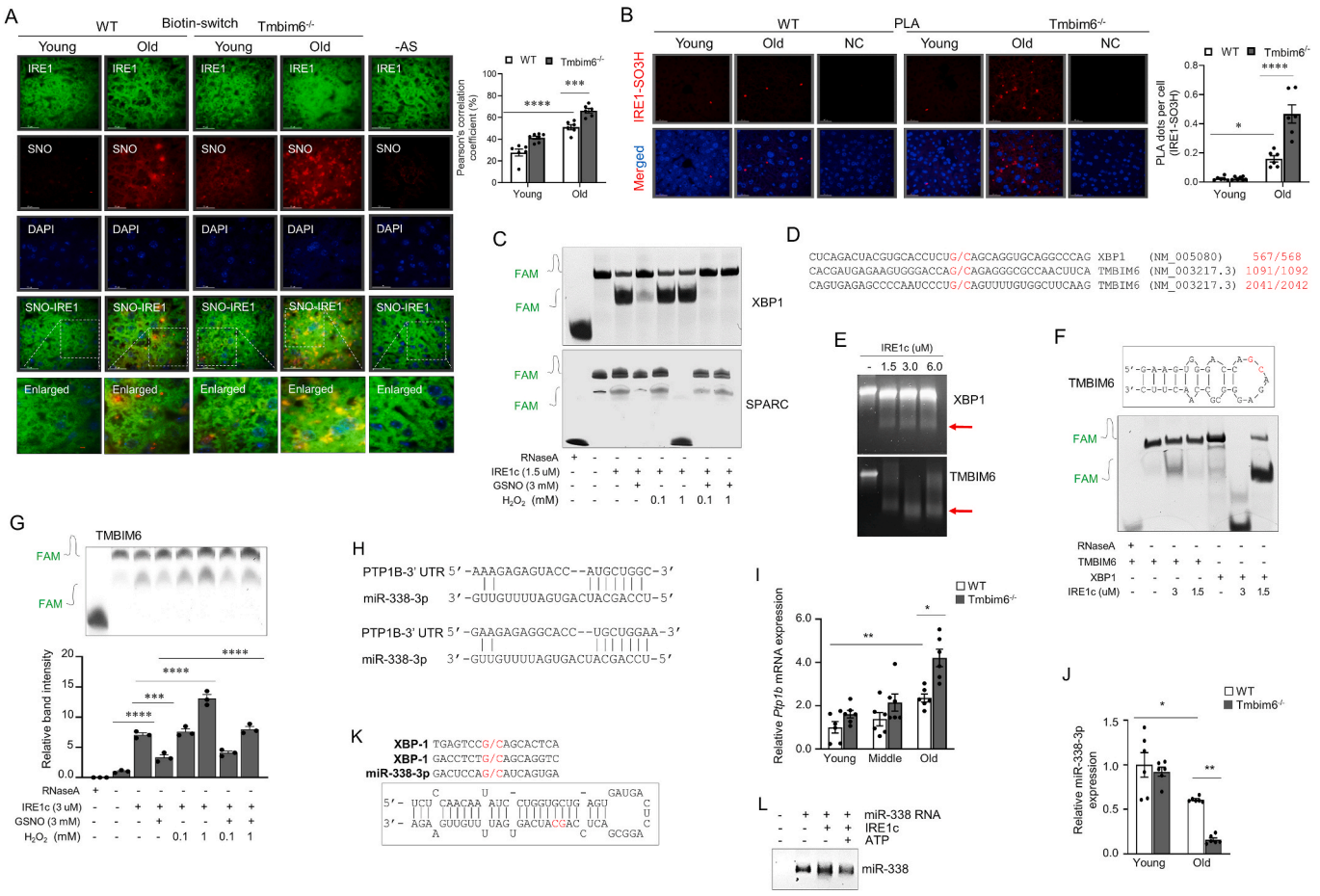

Fig. 4. TMBIM6 deficiency in aging increases redox-mediated post-translational modifications of IRE1α in vivo. (A) Representative images for S-nitrosylated IRE1α in the livers from young and old WT and TMBIM6$^{-/-}$ mice (magnification 60×, scale bar 25 μm). Green images, IRE1α; red, S-nitrosylation; blue, DAPI; SNO-IRE1, merged images; -AS, without ascorbic acid (used as a negative control for S-nitrosylation). The bar graph shows the colocalization between IRE1α and nitrosylated proteins (right) (n = 6–7 per group). (B) IRE1α and cysteine sulfonate proximity ligation assay (PLA) in the liver of young and old WT and TMBIM6$^{-/-}$ mice. Red blobs are the indication of PLA-positive cells. Red images, IRE1α sulfonation; blue, DAPI. Magnification 40×, scale bar 25 μm. NC indicates negative control, where only a single antibody (anti-IRE1α) was used. The bar graph shows the graphical representation of the number of dots per cell of IRE1 sulfonation (below). (C) Urea polyacrylamide gel electrophoresis of sXBP1 and SPARC (as RIDD) substrate with FAM cleaved by IRE1c with GSNO (nitrosylation) and H_2O_2 (sulfonation) donor. RNase A was used as a control. (D) Sequence motif of XBP1 and TMBIM6 with their potential IRE1α cleavage sites (G/C sites marked with red color). (E) In vitro IRE1α-mediated TMBIM6 cleavage assay. In vitro–transcribed TMBIM6 and XBP1 RNA were incubated with or without recombinant IRE1α protein in the reaction buffer. The cleavage reaction products were resolved on an agarose gel. (F) Predicted secondary structures of TMBIM6 with their potential IRE1α cleavage sites (upper) and urea polyacrylamide gel electrophoresis of TMBIM6 substrate with FAM cleaved by IRE1c. (G) Urea polyacrylamide gel electrophoresis of TMBIM6 substrate with FAM cleaved by IRE1c with GSNO and H_2O_2 donor. The bar graph (below) shows the relative band intensity to control (n = 3 independent experiments). (H) Sequence motif of miR-338-3p binding sites to PTP1B. (I–J) The mRNA expression of Ptp1b (I) and miR-338 (J) were analyzed by real-time PCR in the liver of mice (n = 6 mice per group). (K) Sequence motif for the IRE1α cleavage sites (upper) and predicted secondary structures of miR-338b with their potential IRE1α cleavage sites (G/C sites marked with red arrows). (L) In vitro IRE1α-mediated miR-338b cleavage assay was performed. All the data are represented as mean ± S.E.M. *p < 0.05, **p < 0.01, ***p < 0.001, ****p < 0.0001 indicate the significant differences among the groups. (For interpretation of the references to color in this figure legend, the reader is referred to the Web version of this article.)

SNO-IRE1α promotes defective IRE1α RNase activity, while SO_3H-IRE1α increases RIDD without affecting XBP1 splicing [21,32]. Therefore, we performed an in vitro cleavage assay [21] to detect the effect of SNO and SO_3H on XBP1 and RIDD processing using a fluorescence resonance energy transfer (FRET)–quenched XBP1 and SPARC (secreted protein acidic and rich in cysteine) RNA minisubstrate, and a purified human IRE1α (amino acids 465–977, IRE1c). GSNO (a nitric oxide donor to induce S-nitrosylation) treatment impaired the IRE1c-mediated endoribonuclease activity (XBP1 splicing and RIDD) (Fig. 4C), but noticeably, H_2O_2 as a chemical donor (for the generation of ROS and to induce S-sulfonation) increased the cleavage of SPARC, a known RIDD target gene (Fig. 4C, lower panel). Co-treatment of GSNO and H_2O_2 completely inhibited XBP1 splicing, but increased SPARC cleavage (Fig. 4C), which indicates SNO or SO_3H of IRE1 affects the downstream signaling by impairing XBP1 splicing and increasing RIDD activity, respectively.

Since we observed decreased mRNA expression of TMBIM6 (Fig. 1F) and increased SNO and SO_3H of IRE1 in aging mice, therefore, we sought to identify whether IRE1c degrades TMBIM6 as like XBP1 or RIDD. In the TMBIM6 sequence, G/C splicing sites were predicted to be within the stem-loop of the secondary structures (Fig. 4D). Here, we observed that TMBIM6 was highly degraded during IRE1c treatment in a dose-dependent manner (Fig. 4E and F), which indicates that TMBIM6 is a substrate of RIDD. IRE1-mediated XBP1 splicing was also confirmed to have a dose-dependent response (Fig. 4E and F). The degradation of TMBIM6 was also increased with the treatment of H_2O_2 but was intact in GSNO treated condition (Fig. 4G). These results indicate that IRE1-mediated RIDD activity decreases TMBIM6 function. These data further suggest IRE1α as a SNO and SO_3H target protein, which upon associates and alters the function of IRE1α and affects its downstream

molecules, thereby impairing overall ER homeostasis.

We found that the phosphorylation of PERK, another key ER stress sensor, was significantly decreased in old Tmbim6$^{-/-}$ mice than old WT mice (Fig. 3B). The phosphorylation of PERK has been reported to be decreased by protein-tyrosine phosphatase 1B (PTP1B), which was suppressed by miR-338-3p through binding to its 3′-untranslated regions [33,34] (Fig. 4H). Thus, we examined the expression of PTP1B and found that the mRNA expression of PTP1B was increased in old WT and significantly increased in Tmbim6$^{-/-}$ old mice (Fig. 4I). MiR-338-3p was significantly decreased in Tmbim6$^{-/-}$ old mice than old WT mice (Fig. 4J). Previous reports demonstrate that miRNA cleavage by the IRE1α RNase activity [35,36]. We performed an in vitro IRE1α mediated miRNA cleavage assay to determine whether miR-338-3p is degraded by IRE1α RNase activity. As shown in Fig. 4K, the miR-338-3p sequence has G/C splicing sites within the stem-loop of the secondary structures. The miR-338 was verified to be degraded in the presence of ATP and the recombinant IRE1c protein (Fig. 4L), indicating that IRE1α-RIDD suppresses the production of miR-338, so affecting PTP1B and its target protein PERK.

3.5. Overexpression of TMBIM6 regulates senescence and lipid accumulation by reducing nitro-oxidative stress and ER stress in vitro

To better understand the influence of TMBIM6 in lipid accumulation, nitro-oxidative stress, senescence, and ER stress response in vitro, we developed a stable cell line expressing TMBIM6 in human hepatic Hep3B and HepG2 cells (Figs. 5A, S6A). TMBIM6 expressing cells showed reduced ROS and RNS generation (indicated by DHE and DHR-123 fluorescence) than empty vector cells under different stress stimuli (Fig. 5B and C). Lipid accumulation (Fig. 5D) and senescence markers (CellEvent senescence green probe fluorescence and SA-β-gal-positive stained cells) were markedly diminished in TMBIM6 expressed cells under different conditions (Fig. 5E, S6B–S6D). Furthermore, the expression of ER stress elements such as GRP78, p-IRE1α, sXBP1, CHOP, and p-JNK (Fig. 5F, S7A) and cleaved form of caspases 12 and 7 (Fig. 5G, S7B) were reduced in TMBIM6 expressed hepatic cell lines. Under stress

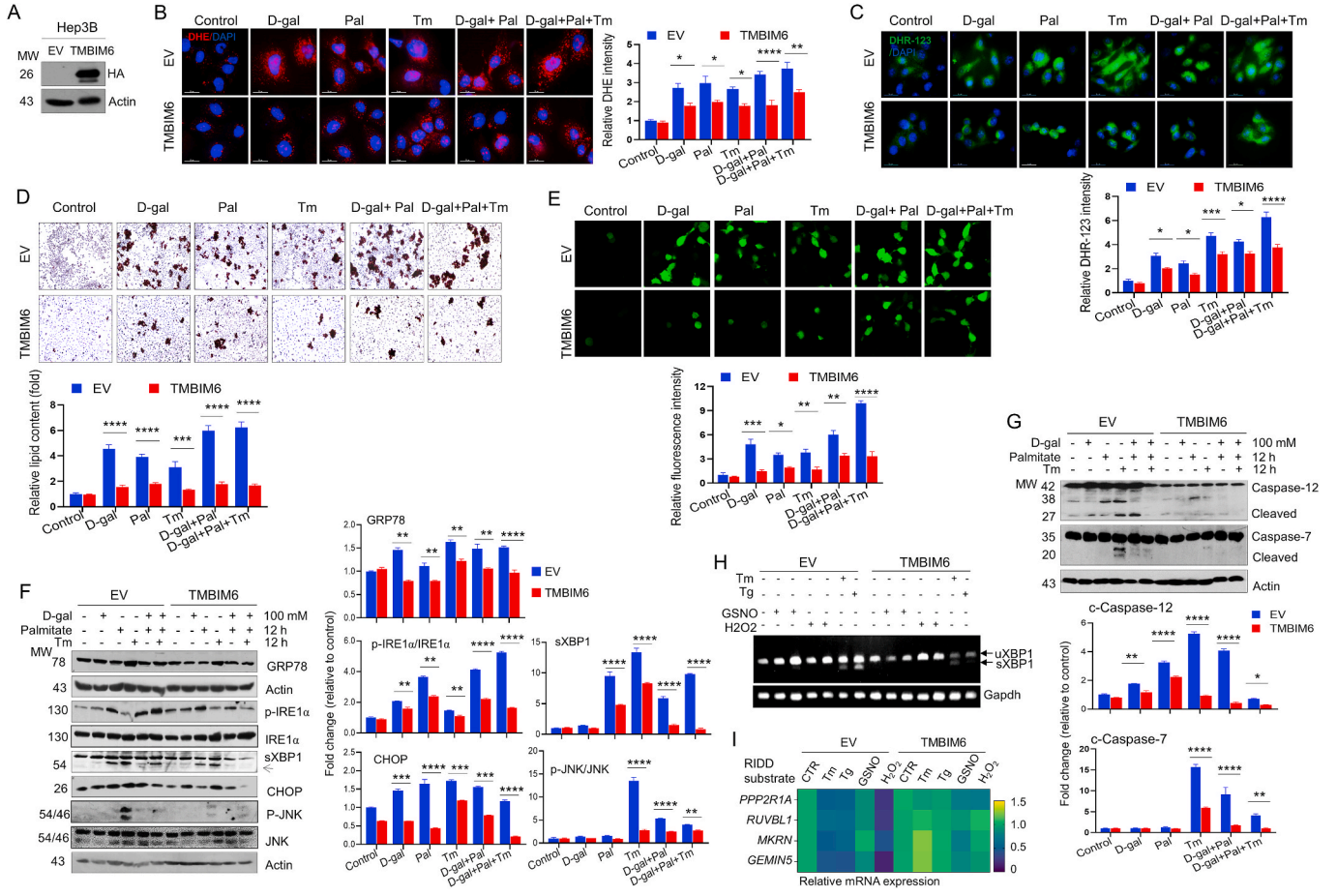

Fig. 5. Overexpression of TMBIM6 regulates senescence and lipid accumulation by reducing nitro-oxidative stress and ER stress in vitro. (A) TMBIM6 protein was overexpressed with a C-terminal HA tag in Hep3B human liver cells. HA expression was assessed by Western blot to demonstrate the stable expression of TMBIM6. (B–C) Hep3B empty vector (EV) and TMBIM6 expressing cells were treated with different stress stimuli such as D-galactose (senescence inducer, 100 mM for 48 h, D-gal), palmitate (lipid inducer, 250 μM for 12 h, Pal), tunicamycin (ER stress inducer, 5 μg/mL for 12 h, Tm), D-galactose and palmitate, and combined treatment of D-galactose, palmitate, and tunicamycin. Dihydroethidium (DHE) (B) and dihydrorhodamine-123 (DHR-123) (C) fluorescence staining was performed and cells were analyzed by confocal microscopy (Magnification: 60×, Bar: 25 μm). The bar graph shows the relative fluorescence intensity (n = 5 per group). (D) Oil Red 'O' staining was performed in EV and HA-TMBIM6 overexpressed Hep3B cells under various stress stimuli treatment (n = 3 per group). (E) Senescent cells staining using CellEvent senescence probe was performed in EV and TMBIM6-overexpressed Hep3B cells under various stress stimuli. Senescent cells developed green fluorescence. The bar graph (right) shows the relative fluorescence intensity to control (n = 3 independent experiments). (F–G) Western blot was performed to examine ER stress response (F) and caspase activation (G) in stimuli-treated EV and HA-TMBIM6-expressed Hep3B cells (n = 3 per group). Actin was used for the loading control. (H) EV and HA-TMBIM6 Hep3B cells were treated with tunicamycin and thapsigargin (2 μM for 12 h), GSNO (100 μM for 1 h and 2 h), and H_2O_2 (500 μM for 2 h and 6 h). RT-PCR was performed for the detection of splicing XBP1. (I) Real-time PCR was performed to detect the gene expression of the RIDD substrates. All the data are represented as mean ± S.E.M. *p < 0.05, **p < 0.01, ***p < 0.001, ****p < 0.0001, indicates the significant differences among the groups. (For interpretation of the references to color in this figure legend, the reader is referred to the Web version of this article.)

conditions, endogenous or exogenous TMBIM6 mRNA expression was not changed (Fig. S7C). Overall, these data suggest that TMBIM6 can regulate stress-induced lipid accumulation, senescence, ER stress, and its mediated apoptosis.

To demonstrate the effects of SNO and SO_3H on IRE1 RNase activity by TMBIM6, we first examined the expression of sXBP1 and RIDD substrates in GSNO/H_2O_2 treated vector and TMBIM6 expressing Hep3B cells. We observed that only Tm and Tg induced high expression of sXBP1 mRNA in vector cells but decreased in TMBIM6 overexpressed cells (Fig. 5H) which is consistent with previous findings [37] indicating that TMBIM6 regulates ER stress. No induction of sXBP1 was observed in GSNO-, H_2O_2-treated vectors, and TMBIM6 expressing cells (Fig. 5H). The expressions of IRE1α-RIDD targeted mRNAs, including PPP2R1A, RUVBL1, MKRN, and GEMIN5 were decreased in H_2O_2-treated vector cells, not in TMBIM6 expressing cells (Fig. 5I). Next, sXBP1 was highly translocated to the nucleus under ER stress (Tm, Tg treatment) in vector cells and was reduced in TMBIM6 expressed cells. Interestingly, GSNO could not increase the nXBP1 in vector cells but increased in the TMBIM6 expressed cells. A modest increase of nXBP1 was observed in H_2O_2-treated cells while nXBP1 was maintained or decreased in TMBIM6 expressed cells (Fig. S7D). To further evaluate how the TMBIM6 maintains XBP1 homeostasis, we investigated the interaction between TMBIM6 and IRE1α via in situ PLA. We observed higher interaction between TMBIM6 and IRE1α in all treated conditions (Fig. S7E), suggesting TMBIM6 regulates IRE1α signaling through its binding. This observation is consistent with the previous report [38].

Additionally, we constructed the mutant C931S of IRE1α and transfected it in Hep3B cells. These mutant cells were treated with D-galactose and assessed for senescent cells (SNCs) using CellEvent Senescence Green Probe kit. The transfected cells with IRE1α WT showed a higher

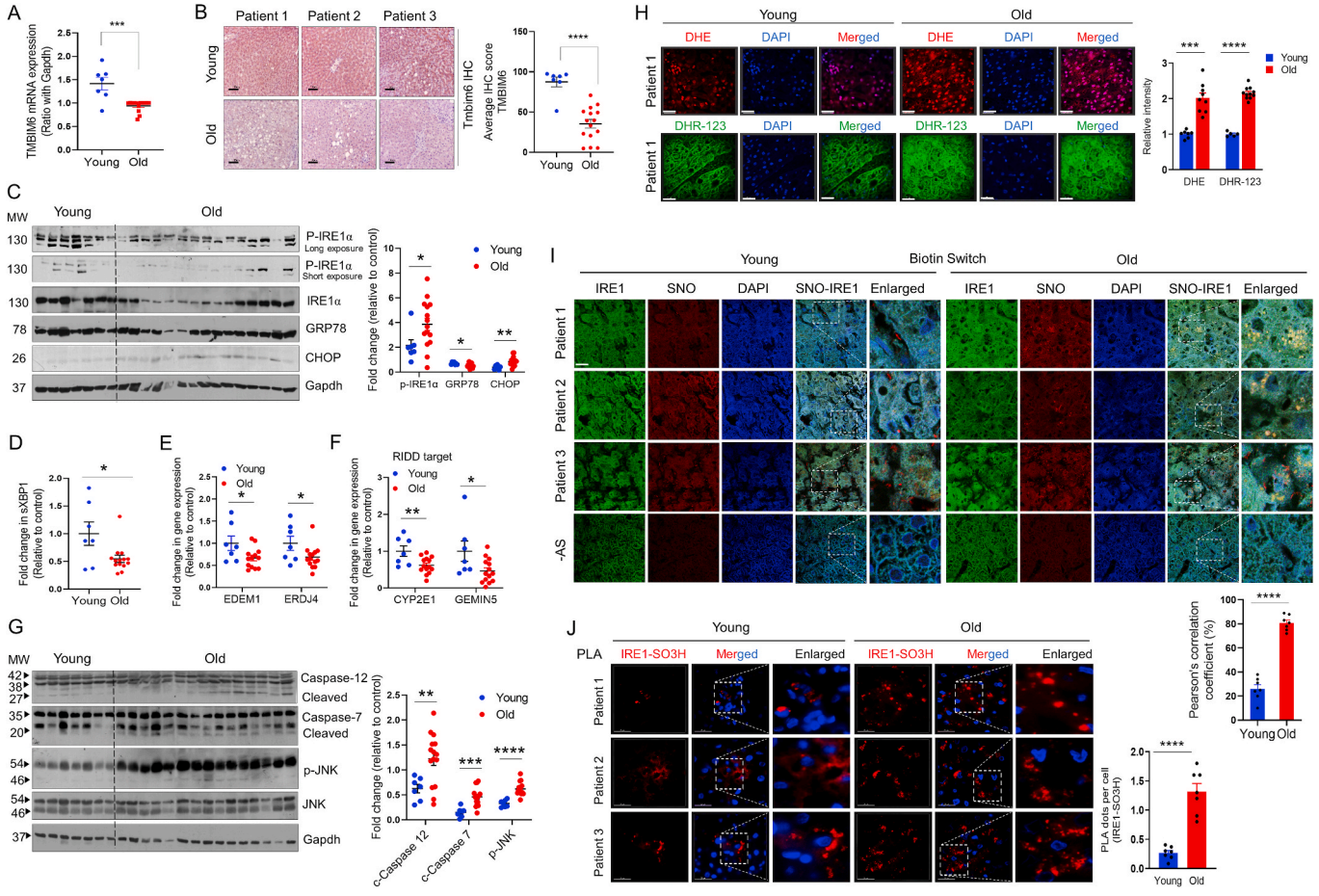

Fig. 6. Aging decreases TMBIM6 expression, induces aberrant UPR expression, S-nitrosylation, and sulfonation of IRE1α in human liver. (A) TMBIM6 mRNA expression and (B) protein expression were analyzed by real-time PCR and immunohistochemistry respectively in young (n = 7) and old human liver tissues (n = 15). (C) Western blotting was performed to check the expression of ER stress response elements p-IRE1, IRE1, GRP78, and CHOP. GAPDH was used as a loading control. Densitometry analysis is shown in the graph (right). (D) The mRNA expression of sXBP1 was analyzed by real-time PCR. (E) The mRNA expression of XBP1 target genes such as EDEM1 and ERDJ4 were measured by real-time PCR. (F) The mRNA expression of the IRE1α-dependent decay (RIDD) target genes such as CYP2E1 and GEMIN5 were examined in the human patient liver samples and analyzed by real-time PCR. (G) Western blotting was performed to check the expression of ER stress-apoptosis-related proteins such as caspase 12, caspase 7, p-JNK, and JNK. GAPDH was used as a loading control. (H) Dihydroethidium (DHE) and Dihydrorhodamine-123 (DHR-123) fluorescence staining were performed in liver sections of young and old patients using confocal microscopy. Red fluorescence indicates DHE positive cells, green fluorescence indicates DHR-123 positive cells, and blue fluorescence indicates DAPI for nuclear staining. The bar graph (right) shows the intensity (n = 7–9 for DHE, n = 5–11 for DHR-123). Magnification: 40×, Scale bar: 25 μm. (I) Representative images for S-nitrosylated IRE1α in the livers from young and old patients (magnification 40×, scale bar 25 μm). S-nitrosylation staining was performed by a modified in situ biotin switch method. Green images, IRE1α; red, S-nitrosylation; blue, DAPI; SNO-IRE1, merged images; -AS, without ascorbic acid (used as a negative control for S-nitrosylation). The bar graph (bottom) shows the colocalization between IRE1α and nitrosylated proteins (n = 7 per group). (J) IRE1α and cysteine sulfonate proximity ligation assay (PLA) in the liver of young and old patients' livers. Red blots are the indication of PLA-positive cells. Red images, IRE1α sulfonation; blue, DAPI. Magnification 60×, scale bar 25 μm. The bar graph (right) shows the graphical representation of the number of dots per cell of IRE1 sulfonation (n = 7 per group). All the data are represented as mean ± S.E.M. *p < 0.05, **p < 0.01, ***p < 0.001, ****p < 0.0001, indicates the significant differences among the groups (n = 7/young, and n = 15/old patients in all experiments). (For interpretation of the references to color in this figure legend, the reader is referred to the Web version of this article.)

number (high fluorescence) of SNCs upon D-galactose treatment, while the cells with IRE1α C931S showed a limited number of SNCs in vector and TMBIM6 overexpressing cells (Fig. S7F). Collectively, these results suggest that TMBIM6 can inhibit the modifications of IRE1α through its close interaction, succeeding in cell death protection.

3.6. Aging exaggerates lipid accumulation, aberrant UPR expression, S-nitrosylation, and sulfonation of IRE1α in human liver

To investigate the mechanisms by which TMBIM6 deficiency increases lipid accumulation in human aging liver, normal tissue adjacent to the tumor (NAT) were obtained from the liver cancer patients (young and old) having an average BMI of 24.96 kg/m^2. A recent report suggests that Asians with a BMI of 25 kg/m^2 or less are considered as 'non-obese' NAFLD because they are likely to have steatosis, histological lobular inflammation, or high metabolic risk factors [39]. In this study, the body weight, BMI, and lipid profiles of patients are similar. (Figs. S8A–G). TMBIM6 was significantly less in older patients than the young (Fig. 6A and B). Histological abnormalities including inflammatory cell infiltration and multiple large fat vacuoles were deposited in the liver of aged patients than in younger patients (Fig. S8H). We next evaluated the ER stress markers and found that increased p-IRE1α and CHOP, and decreased GRP78 expressions in old samples compared to the young (Fig. 6C). The mRNA levels of sXBP1 and its target genes (Edem1 and Erdj4) (Fig. 6D and E), and RIDD substrates genes (CYP2E1 and Gemin5) (Fig. 6F) were significantly reduced in aged patients than young patients. To verify whether aged human samples had higher apoptosis similar to the mice model, we evaluated the expression of cleaved 12, caspase 7, and p-JNK. The expression levels of these proteins significantly increased in aged tissue, suggesting that older tissue undergo apoptosis much faster than the young. (Fig. 6G). Since the sXBP1 was also decreased in aging patients as in the mouse model along with increased ROS and RNS (Fig. 6H, S8I, S8J). We further evaluated the cysteine modifications in young and aged liver tissues. We noticed high levels of SNO-IRE1α and SO_3H-IRE1α in the liver samples of the aged patient than the younger ones (Fig. 6I and J). Altogether, these data

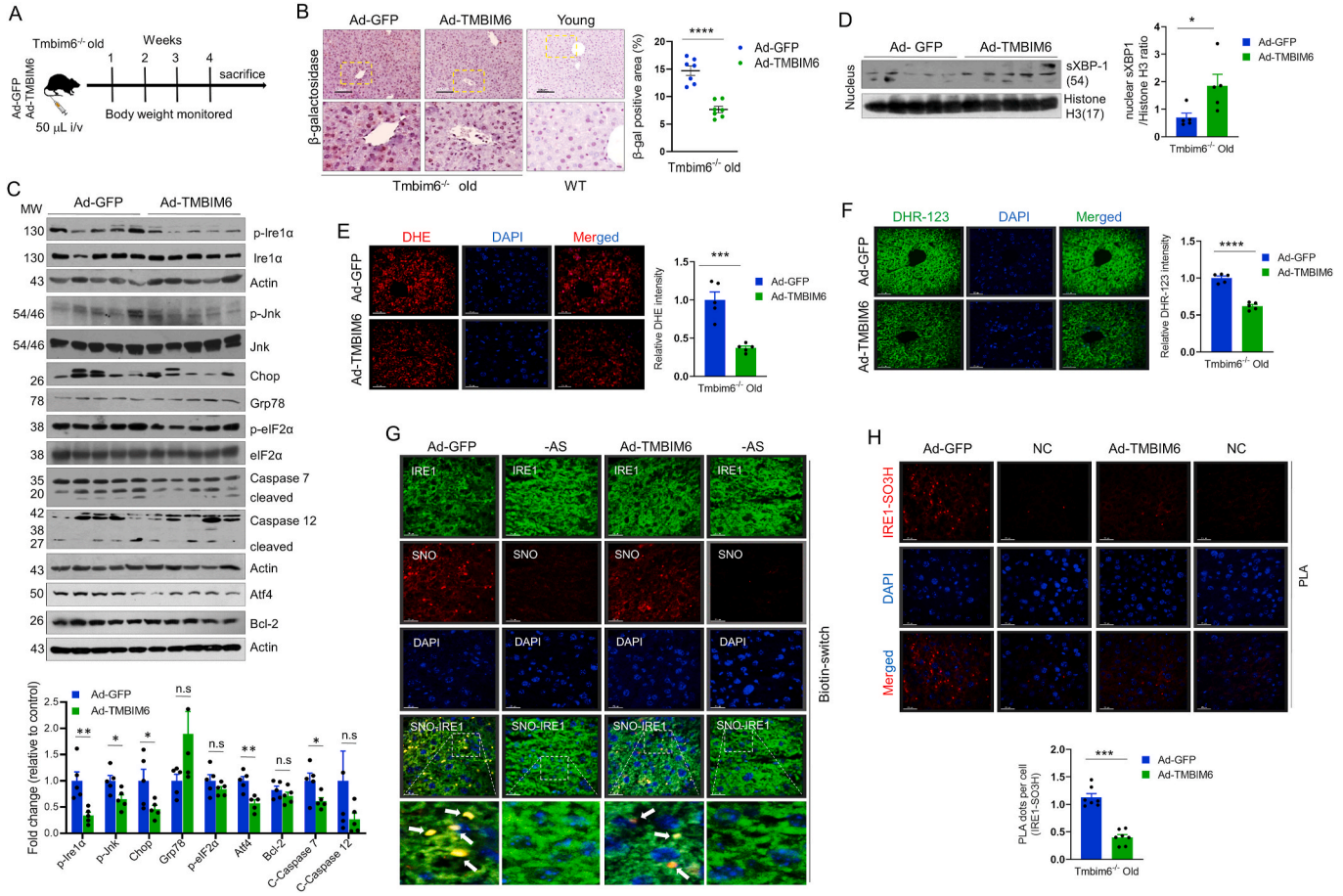

Fig. 7. Adenovirus-mediated TMBIM6 delivery to liver reduced aging-associated lipid accumulation in TMBIM6$^{-/-}$ mice. (A) Adenoviral vector expressing TMBIM6 was injected via tail vein injection in TMBIM6$^{-/-}$ old mice. TMBIM6$^{-/-}$ old mice were infected with Ad-GFP and Ad-TMBIM6 at 1.0 × 10^9 PFU virus particles and kept for 4 weeks. (B) Images were obtained by beta-galactosidase immunostaining (magnification: 20×, lower panel: enlarged area) (n = 7 per group). (C) The expression of the indicated proteins was examined by immunoblotting using specific antibodies. Actin was used as a loading control. The bar graph (lower) shows the densitometry analysis from the Western blot (n = 5 per group). (D) Nucleus was isolated from whole liver tissue from Ad-GFP and Ad-TMBIM6 old mice and sXBP1 expression was examined by Western blot (12% gel). Histone H3 (nuclear localization marker) was used as a loading control. The bar graph (below) shows the average intensity and was compared among the groups (n = 5 per group). (E–F) DHE and DHR-123 fluorescence staining for liver sections were performed and imaged by confocal microscopy. The bar graph (right) shows the relative fluorescence intensities of DHE, and DHR-123 in Ad-GFP and Ad-TMBIM6 old mice (n = 5 per group). (G) S-nitrosylation of IRE1α was determined in the liver sections using a modified biotin-switch method (see protocol in the method section). (-AS) indicates without ascorbate and used as a negative control. (H) Duolink in situ proximity ligation assay was performed in the liver sections to determine the proximity between IRE1α and sulfonation. Liver sections from Ad-GFP mice and Ad-TMBIM6 were incubated with mouse anti-IRE1α and rabbit anti-cysteine sulfonate antibodies and analyzed using the protocol as explained in the method section. NC indicates negative control, where only IRE1α antibody was incubated. The bar graph (bottom) shows the graphical representation of the number of dots per cell of IRE1 sulfonation (n = 7 per group). All the data are represented as mean ± S.E.M. *p < 0.05, **p < 0.01, ***p < 0.001, ****p < 0.0001, indicates the significant differences among the groups. n.s; not significant.

suggest that TMBIM6 deficiency induces impairment of ER stress response during aging via redox-mediated S-nitrosylation or sulfonation of IRE1α.

3.7. Adenovirus-mediated TMBIM6 delivery to liver reduced aging-associated lipid accumulation in TMBIM6$^{-/-}$ mice

To further delineate whether TMBIM6 reexpression in the liver of TMBIM6$^{-/-}$ old mice can improve steatosis, we performed a rescue experiment using adenovirus-mediated TMBIM6 gene delivery system (Fig. 7A). TMBIM6 delivery was confirmed by hemagglutinin (HA) expression (Fig. S9C). After injection, mice body weight remained consistent, and no significant differences were observed between Ad-GFP and Ad-TMBIM6 (Figs. S9A and S9B). Liver size and weight (Figs. S9B and S9D), serum lipid profiles (Figs. S9E–S9H), as well as lipid vacuoles and fat droplets (Figs. S9I and S9J), were markedly reduced in Ad-TMBIM6 infected mice than GFP alone, suggests TMBIM6 as a regulator of aging-associated hepatic steatosis. Furthermore, TMBIM6 re-expression reversed the senescence that occurred in TMBIM6$^{-/-}$ old mice (Fig. 7B). Interestingly, TMBIM6 re-expression inhibited the expression of p-IRE1α, p-JNK, CHOP, ATF4, and cleaved caspase 7 than GFP-infected old mice (Fig. 7C). Total sXBP1 mRNA was unchanged (Fig. S9K), but the nuclear expression of sXBP1 (Fig. 7D) and its target genes (Fig. S9L and S9M) were increased in Ad-TMBIM6 infected old mice than GFP infected mice, indicating the potential ability of TMBIM6 in navigating cell death and cell survival to regulate ER homeostasis. We further found that ROS and RNS were decreased in Ad-TMBIM6 than Ad-GFP (Fig. 7E and F). Further, we validated that overexpression of TMBIM6 decreases aging-induced SNO and SO_3H of IRE1α in the liver sections of TMBIM6$^{-/-}$ old mice (Fig. 7G and H). These observations suggest TMBIM6 as a regulator of redox-mediated PTMs of IRE1α and its potentials in reducing age-associated lipid accumulation.

4. Discussion

The role of TMBIM6 and its associated mechanism in aging has not been extensively studied. Here, we demonstrated that deficiency of TMBIM6in aging humans and mice showed increased redox-mediated PTMs such as S-nitrosylation and sulfonation of IRE1α, the most conserved ER membrane protein. PTM in IRE1α leads to a disruption of the IRE1α downstream signaling causing ER stress response failure. Intriguingly, TMBIM6$^{-/-}$ mice developed steatosis from middle age even under normal nutritional conditions than WT mice under the same conditions.

In this study, the disruption of adaptive capacity to cope with the metabolic demands of aging process is found to be regulated by TMBIM6. The activity and expression of many UPR components reduce and accelerates aging and age-associated disorders [40,41]. In our study, aged TMBIM6$^{-/-}$ mice showed reduced expression of adaptive proteins. However, proteins responsible for the apoptotic process were significantly high, suggesting that TMBIM6 has regulatory functions towards impaired UPR induced by aging (Figs. 3B, 2G). We speculated that the decreased UPR components in TMBIM6$^{-/-}$ old mice may not defend the stress response and led to apoptosis, suggesting that inactivation of UPR protective pathways may exacerbate age-associated steatosis. Previous studies showed that JNK and CHOP activation is greater in aged hepatocytes, indicating the role of JNK signaling in ER stress-mediated cell death [42,43]. Similarly, in old TMBIM6$^{-/-}$ mice, strong expression of CHOP, suppressed anti-apoptotic proteins like BCL-2, Bcl-xL, and Mcl-1, and increased caspase activation were observed. These data are consistent with an earlier report suggesting that overexpression of CHOP leads to downregulation of pro-survival BCL-2 and sensitizes apoptosis during ER stress [44]. It has been indicated that one of the pathways to prolong longevity is to activate a cellular stress response that recognizes misfolded proteins and regulates cellular homeostasis [45]. Remarkably, the lack of TMBIM6 in aging does not activate the downstream signaling molecules from ER stress sensors and distinctively impairs the UPR, suggesting an escalated ER stress, termed as 'ER stress sensing or response failure' [5,46].

Aging is a complex process and involves multiple mechanisms. We believe that age-associated steatosis can be limited by maintaining overall ER homeostasis. More specifically, though the lack of TMBIM6 in old mice induced p-IRE1α and activated its downstream p-JNK and increased RIDD, it did not induce its other downstream sXBP1, indicating that TMBIM6$^{-/-}$ reduces hepatic cell survival in old age (Fig. 3B, 3D-G). The ER stress response failure disrupted the downstream target gene sXBP1 and led to the accumulation of ubiquitinated proteins and HMWC of PDI, collectively responsible for increased ERAD dysfunction (Figs. S4D and S4E). In search of the mechanism, we demonstrated that severe redox-mediated PTMs of IRE1α impairs ER function and prolongs ER stress in human and mice aging models. Further, these PTMs of IRE1α were enhanced under TMBIM6 deficiency conditions (Figs. 4, 6 and 7). We performed an in vitro cleavage assay to gain insights into the aftermath of severe SNO and SO_3H of IRE1α in downstream target molecules. Treatment with NO donor (GSNO-induced S-nitrosylation) impaired IRE1-mediated cleavage of XBP1 mRNA, whereas H_2O_2 (severe ROS-induced sulfonation) increased the cleavage of SPARC (Fig. 4C). These data indicate that SNO or SO_3H of IRE1α affects its endoribonuclease activity, thereby impairs sXBP1 or increases RIDD activity, leading to cell death. More importantly, SO_3H-IRE1α increased TMBIM6 decay (Fig. 4F and G). Thus, TMBIM6 is suggested as IRE1-mediated RIDD substrate.

S-nitrosylation of IRE1α inhibits its endoribonuclease activity to attenuate sXBP1 production or nuclear translocation, thereby impeding downstream targets, such as reduced ER chaperones and ERAD dysfunction or defective autophagy, which are essential for maintaining ER homeostasis. We recently recognized that TMBIM6 has the potential to enhance autophagy [47] and is involved in cell survival by regulating the activation of AKT [48]. Moreover, TMBIM6$^{-/-}$ can lead to a defective degradation system and increase cell death under severe stress conditions such as aging. Impaired autophagy signaling has been linked with impaired adaptive UPR in the obesity model, where nitrosative stress plays a role in inhibiting IRE1α-mediated XBP1 splicing [21,49]. Cysteine residues 931 (C931) and 951 (C951) of IRE1α peptides located in the RNase domain are identified for the relevant S-nitrosylation that impairs IRE1α RNase enzyme activity, eventually attenuating XBP1 splicing [21,50]. Recently, we have discovered that IRE1α is S-sulfonated at C715 and C762, which is mediated by a high level of ROS and can trigger ER stress-induced apoptosis [32]. In contrast, increased iNOS-induced metaflammation is associated with impaired XBP1 processing in obesity [21], which is consistent with our findings in the age-associated steatosis model (Fig. S5D). A defective nuclear translocation of sXBP1 has been observed in several pathological conditions such as obesity, insulin resistance, and diabetic nephropathy [51–53], in which the interaction between sXBP1 and regulatory subunits of PI3K (p85α and p85β) was impaired, aggravating the pathogenesis of diseases [4,51]. Previous studies identified TMBIM6 as a regulator of the pharmacologically-induced ER stress response (particularly p-IRE1α -mediated XBP1 splicing) [37,38]. However, our study uncovers a long unresolved question of how TMBIM6 promotes cell survival even by inhibiting sXBP1 during ER stress condition. Our data revealed that TMBIM6 navigates IRE1α-mediated XBP1 splicing or/and RIDD, depending on redox-mediated PTMs of IRE1α into SNO or SO_3H, which generally facilitate the alteration of IRE1α function. The competitive stimulation of SNO and SO_3H determines the activation or inhibition of IRE1 RNase splicing activity or RIDD, which are critical for sensing cell adaptation or death signals. The delivery of the TMBIM6 gene to the liver of old TMBIM6$^{-/-}$ mice have shown promise in regulating steatosis by maintaining redox-associated PTMs and ER homeostasis (Fig. 7).

Similar to IRE1α, there were some disturbances in the PERK-eIF2α-ATF4 axis (Figs. 3B, 4H) in aging WT and TMBIM6$^{-/-}$ mice. NO-induced phosphorylation of PERK and eIF2α was shown in the previous report

[50]. However, our results demonstrate that aging mice showed a decreasing pattern in phosphorylation of PERK and eIF2α. Thus, in this study, we focused on the connection between IRE1α and PERK to explain the ER stress response failure; the disturbance of ER stress signaling axis. We recently reported that strong IRE1α RNase activation by sulfonation caused decay of miR-23b, which contained consensus sequence 'CUG-CAG' as selectively recognizing motif [32]. Several miRNA including miR-17-5p, miR-34a-5p, miR-96-5p, and miR-125b-5p were cleaved by IRE1α RNase activation [36]. In this same manner, miR-338-3p was degraded by IRE1α and increased gene expression of PTP1B (Fig. 4I and J). PTP1B decrease the phosphorylation of tyrosine 615 in kinase domain and reduce overall serine/threonine phosphorylation of PERK [54]. Since the IRE1α-RIDD-miRNA axis also interrupts the PERK signaling through the targeted PTP1B, overall ER stress response impairment seems to be accelerated during aging, indicating that the inhibition of IRE1α modifications might be one of preventing or controlling strategy against aging-associated metabolic disorders.

In summary, age-associated maladaptive UPR and the PTMs of IRE1α 'SO_3H and SNO of IRE1α'–linked RIDD-TMBIM6 decay and XBP-1 splicing inhibition are involved in age-associated hepatic steatosis. This study suggests that depletion of the ER-resident molecule TMBIM6 induces impaired ER proteostasis and is unresponsive to the downstream UPR signaling, demonstrating that TMBIM6 maintains overall ER homeostasis. Future studies are warranted to understand how TMBIM6 navigates the paradox between IRE1-mediated RIDD activity and IRE1-sXBP1-mediated homeostasis and cell survival.

Declaration of competing interest

The authors declare that they have no known competing financial interests or personal relationships that could have appeared to influence the work reported in this paper.

Acknowledgements

We thank Yong Liu (University of the Chinese Academy of Sciences, China) for kindly providing IRE1α plasmid.

Appendix A. Supplementary data

Supplementary data to this article can be found online at https://doi.org/10.1016/j.redox.2021.102128.

Author's contributions

KRB, HKK and HJC conceived and designed the study and experiments involved. KRB, HKK, MC, MMUR, and JSK performed the experiments. KRB, HKK, HJC, and HRK analyzed the data. KRB wrote the manuscript. HJC and HRK supervised the study, validated the results and provided technical guidance for all aspects of the project. All authors read, commented and approved the final manuscript.

Financial support

This work was supported by the National Research Foundation of Korea (2020R1A2B5B03094896, 2017R1E1A1A01073796, 2017M3A9G7072719, 2017M3A9E4047243, and 2020R1I1A1A01069205).

References

[1] G. Martinez, S. Khatiwada, M. Costa-Mattioli, C. Hetz, ER proteostasis control of neuronal physiology and synaptic function, Trends Neurosci. 41 (9) (2018) 610–624.
[2] J.H. Lin, P. Walter, T.S. Yen, Endoplasmic reticulum stress in disease pathogenesis, Annu. Rev. Pathol. 3 (2008) 399–425.
[3] C. Hetz, F.R. Papa, The unfolded protein response and cell fate control, Mol. Cell 69 (2) (2018) 169–181.
[4] K.R. Bhattarai, T.A. Riaz, H.R. Kim, H.J. Chae, The aftermath of the interplay between the endoplasmic reticulum stress response and redox signaling, Exp. Mol. Med. (2021).
[5] K.R. Bhattarai, M. Chaudhary, H.R. Kim, H.J. Chae, Endoplasmic reticulum (ER) stress response failure in diseases, Trends Cell Biol. (2020).
[6] M.K. Brown, N. Naidoo, The endoplasmic reticulum stress response in aging and age-related diseases, Front. Physiol. 3 (2012) 263.
[7] F. Bonomini, L.F. Rodella, R. Rezzani, Metabolic syndrome, aging and involvement of oxidative stress, Aging Dis. 6 (2) (2015) 109–120.
[8] V.J. Lavallard, P. Gual, Autophagy and non-alcoholic fatty liver disease, BioMed Res. Int. 2014 (2014) 120179.
[9] R. Singh, S. Kaushik, Y. Wang, Y. Xiang, I. Novak, M. Komatsu, K. Tanaka, A. M. Cuervo, M.J. Czaja, Autophagy regulates lipid metabolism, Nature 458 (7242) (2009) 1131–1135.
[10] F. Sheedfar, S. Di Biase, D. Koonen, M. Vinciguerra, Liver diseases and aging: friends or foes? Aging Cell 12 (6) (2013) 950–954.
[11] H.Y. Lee, G.H. Lee, K.R. Bhattarai, B.H. Park, S.H. Koo, H.R. Kim, H.J. Chae, Bax Inhibitor-1 regulates hepatic lipid accumulation via ApoB secretion, Sci. Rep. 6 (2016) 27799.
[12] Z.M. Younossi, A.B. Koenig, D. Abdelatif, Y. Fazel, L. Henry, M. Wymer, Global epidemiology of nonalcoholic fatty liver disease-Meta-analytic assessment of prevalence, incidence, and outcomes, Hepatology 64 (1) (2016) 73–84.
[13] M.H. Le, P. Devaki, N.B. Ha, D.W. Jun, H.S. Te, R.C. Cheung, M.H. Nguyen, Prevalence of non-alcoholic fatty liver disease and risk factors for advanced fibrosis and mortality in the United States, PloS One 12 (3) (2017), e0173499.
[14] H.J. Chae, H.R. Kim, C. Xu, B. Bailly-Maitre, M. Krajewska, S. Krajewski, S. Banares, J. Cui, M. Digicaylioglu, N. Ke, S. Kitada, E. Monosov, M. Thomas, C. L. Kress, J.R. Babendure, R.Y. Tsien, S.A. Lipton, J.C. Reed, BI-1 regulates an apoptosis pathway linked to endoplasmic reticulum stress, Mol. Cell 15 (3) (2004) 355–366.
[15] Q. Xu, J.C. Reed, Bax inhibitor-1, a mammalian apoptosis suppressor identified by functional screening in yeast, Mol. Cell 1 (3) (1998) 337–346.
[16] J.L. Kuk, T.J. Saunders, L.E. Davidson, R. Ross, Age-related changes in total and regional fat distribution, Ageing Res. Rev. 8 (4) (2009) 339–348.
[17] F. Garawi, K. Devries, N. Thorogood, R. Uauy, Global differences between women and men in the prevalence of obesity: is there an association with gender inequality? Eur. J. Clin. Nutr. 68 (10) (2014) 1101–1106.
[18] G.H. Lee, K.J. Oh, H.R. Kim, H.S. Han, H.Y. Lee, K.G. Park, K.H. Nam, S.H. Koo, H. J. Chae, Effect of BI-1 on insulin resistance through regulation of CYP2E1, Sci. Rep. 6 (2016) 32229.
[19] G.H. Lee, T. Ahn, D.S. Kim, S.J. Park, Y.C. Lee, W.H. Yoo, S.J. Jung, J.S. Yang, S. Kim, A. Muhlrad, Y.R. Seo, S.W. Chae, H.R. Kim, H.J. Chae, Bax inhibitor 1 increases cell adhesion through actin polymerization: involvement of calcium and actin binding, Mol. Cell Biol. 30 (7) (2010) 1800–1813.
[20] J.M. Wang, Y. Qiu, Z.Q. Yang, L. Li, K. Zhang, Inositol-requiring enzyme 1 facilitates diabetic wound healing through modulating MicroRNAs, Diabetes 66 (1) (2017) 177–192.
[21] L. Yang, E.S. Calay, J. Fan, A. Arduini, R.C. Kunz, S.P. Gygi, A. Yalcin, S. Fu, G. S. Hotamisligil, METABOLISM. S-Nitrosylation links obesity-associated inflammation to endoplasmic reticulum dysfunction, Science 349 (6247) (2015) 500–506.
[22] E.G. Bligh, W.J. Dyer, A rapid method of total lipid extraction and purification, Can. J. Biochem. Physiol. 37 (8) (1959) 911–917.
[23] C. Segnani, C. Ippolito, L. Antonioli, C. Pellegrini, C. Blandizzi, A. Dolfi, N. Bernardini, Histochemical detection of collagen fibers by Sirius red/fast green is more sensitive than van Gieson or Sirius red alone in normal and inflamed rat colon, PloS One 10 (12) (2015), e0144630.
[24] K.R. Bhattarai, H.Y. Lee, S.H. Kim, H.R. Kim, H.J. Chae, Ixeris dentata extract increases salivary secretion through the regulation of endoplasmic reticulum stress in a diabetes-induced xerostomia rat model, Int. J. Mol. Sci. 19 (4) (2018).
[25] H.K. Kim, G.H. Lee, K.R. Bhattarai, R.P. Junjappa, H.Y. Lee, M. Handigund, A. Marahatta, B. Bhandary, I.H. Baek, J.S. Pyo, H.K. Kim, O.H. Chai, H.R. Kim, Y. C. Lee, H.J. Chae, PI3Kdelta contributes to ER stress-associated asthma through ER-redox disturbances: the involvement of the RIDD-RIG-I-NF-kappaB axis, Exp. Mol. Med. 50 (2) (2018) e444.
[26] M. Ogrodnik, S. Miwa, T. Tchkonia, D. Tiniakos, C.L. Wilson, A. Lahat, C.P. Day, A. Burt, A. Palmer, Q.M. Anstee, S.N. Grellscheid, J.H.J. Hoeijmakers, S. Barnhoorn, D.A. Mann, T.G. Bird, W.P. Vermeij, J.L. Kirkland, J.F. Passos, T. von Zglinicki, D. Jurk, Cellular senescence drives age-dependent hepatic steatosis, Nat. Commun. 8 (2017) 15691.
[27] L.E. Rikans, K.R. Hornbrook, Lipid peroxidation, antioxidant protection and aging, Biochim. Biophys. Acta 1362 (2–3) (1997) 116–127.
[28] H. Kenche, C.J. Baty, K. Vedagiri, S.D. Shapiro, A. Blumental-Perry, Cigarette smoking affects oxidative protein folding in endoplasmic reticulum by modifying protein disulfide isomerase, Faseb. J. 27 (3) (2013) 965–977.
[29] T. Nakamura, S. Tu, M.W. Akhtar, C.R. Sunico, S. Okamoto, S.A. Lipton, Aberrant protein s-nitrosylation in neurodegenerative diseases, Neuron 78 (4) (2013) 596–614.
[30] T. Uehara, T. Nakamura, D. Yao, Z.-Q. Shi, Z. Gu, Y. Ma, E. Masliah, Y. Nomura, S. A. Lipton, S-nitrosylated protein-disulphide isomerase links protein misfolding to neurodegeneration, Nature 441 (7092) (2006) 513–517.
[31] P.A. Kramer, J. Duan, W.J. Qian, D.J. Marcinek, The measurement of reversible redox dependent post-translational modifications and their regulation of mitochondrial and skeletal muscle function, Front. Physiol. 6 (2015) 347.

[32] H.K. Kim, H.Y. Lee, T.A. Riaz, K.R. Bhattarai, M. Chaudhary, J.H. Ahn, J. Jeong, H. R. Kim, H.J. Chae, Chalcone suppresses tumor growth through NOX4-IRE1alpha sulfonation-RIDD-miR-23b axis, Redox Biol. 40 (2021) 101853.
[33] J. Bakke, F.G. Haj, Protein-tyrosine phosphatase 1B substrates and metabolic regulation, Semin. Cell Dev. Biol. 37 (2015) 58–65.
[34] F. Sun, M. Yu, J. Yu, Z. Liu, X. Zhou, Y. Liu, X. Ge, H. Gao, M. Li, X. Jiang, S. Liu, X. Chen, W. Guan, miR-338-3p functions as a tumor suppressor in gastric cancer by targeting PTP1B, Cell Death Dis. 9 (5) (2018) 522.
[35] M. Maurel, E. Chevet, Endoplasmic reticulum stress signaling: the microRNA connection, Am. J. Physiol. Cell Physiol. 304 (12) (2013) C1117–C1126.
[36] J.P. Upton, L. Wang, D. Han, E.S. Wang, N.E. Huskey, L. Lim, M. Truitt, M. T. McManus, D. Ruggero, A. Goga, F.R. Papa, S.A. Oakes, IRE1alpha cleaves select microRNAs during ER stress to derepress translation of proapoptotic Caspase-2, Science 338 (6108) (2012) 818–822.
[37] G.H. Lee, D.S. Kim, H.T. Kim, J.W. Lee, C.H. Chung, T. Ahn, J.M. Lim, I.K. Kim, H. J. Chae, H.R. Kim, Enhanced lysosomal activity is involved in Bax inhibitor-1-induced regulation of the endoplasmic reticulum (ER) stress response and cell death against ER stress: involvement of vacuolar H+-ATPase (V-ATPase), J. Biol. Chem. 286 (28) (2011) 24743–24753.
[38] F. Lisbona, D. Rojas-Rivera, P. Thielen, S. Zamorano, D. Todd, F. Martinon, A. Glavic, C. Kress, J.H. Lin, P. Walter, J.C. Reed, L.H. Glimcher, C. Hetz, BAX inhibitor-1 is a negative regulator of the ER stress sensor IRE1alpha, Mol. Cell 33 (6) (2009) 679–691.
[39] J.G. Fan, S.U. Kim, V.W. Wong, New trends on obesity and NAFLD in Asia, J. Hepatol. 67 (4) (2017) 862–873.
[40] S. Fu, S.M. Watkins, G.S. Hotamisligil, The role of endoplasmic reticulum in hepatic lipid homeostasis and stress signaling, Cell Metabol. 15 (5) (2012) 623–634.
[41] N. Naidoo, The endoplasmic reticulum stress response and aging, Rev. Neurosci. 20 (1) (2009) 23–37.
[42] N.J. Darling, S.J. Cook, The role of MAPK signalling pathways in the response to endoplasmic reticulum stress, Biochim. Biophys. Acta 1843 (10) (2014) 2150–2163.
[43] J. Li, N.J. Holbrook, Elevated gadd153/chop expression and enhanced c-Jun N-terminal protein kinase activation sensitizes aged cells to ER stress, Exp. Gerontol. 39 (5) (2004) 735–744.
[44] Y. Li, Y. Guo, J. Tang, J. Jiang, Z. Chen, New insights into the roles of CHOP-induced apoptosis in ER stress, Acta Biochim. Biophys. Sin. 46 (8) (2014) 629–640.
[45] R.C. Taylor, Aging and the UPR(ER), Brain Res. 1648 (Pt B) (2016) 588–593.
[46] T. Sasako, M. Ohsugi, N. Kubota, S. Itoh, Y. Okazaki, A. Terai, T. Kubota, S. Yamashita, K. Nakatsukasa, T. Kamura, K. Iwayama, K. Tokuyama, H. Kiyonari, Y. Furuta, J. Shibahara, M. Fukayama, K. Enooku, K. Okushin, T. Tsutsumi, R. Tateishi, K. Tobe, H. Asahara, K. Koike, T. Kadowaki, K. Ueki, Hepatic Sdf2l1 controls feeding-induced ER stress and regulates metabolism, Nat. Commun. 10 (1) (2019) 947.
[47] H.K. Kim, G.H. Lee, K.R. Bhattarai, M.S. Lee, S.H. Back, H.R. Kim, H.J. Chae, TMBIM6 (transmembrane BAX inhibitor motif containing 6) enhances autophagy through regulation of lysosomal calcium, Autophagy (2020) 1–18.
[48] H.K. Kim, K.R. Bhattarai, R.P. Junjappa, J.H. Ahn, S.H. Pagire, H.J. Yoo, J. Han, D. Lee, K.W. Kim, H.R. Kim, H.J. Chae, TMBIM6/BI-1 contributes to cancer progression through assembly with mTORC2 and AKT activation, Nat. Commun. 11 (1) (2020) 4012.
[49] Z. Zhang, Q. Qian, M. Li, F. Shao, W.X. Ding, V.A. Lira, S.X. Chen, S.C. Sebag, G. S. Hotamisligil, H. Cao, L. Yang, The unfolded protein response regulates hepatic autophagy by sXBP1-mediated activation of TFEB, Autophagy (2020) 1–15.
[50] R. Nakato, Y. Ohkubo, A. Konishi, M. Shibata, Y. Kaneko, T. Iwawaki, T. Nakamura, S.A. Lipton, T. Uehara, Regulation of the unfolded protein response via S-nitrosylation of sensors of endoplasmic reticulum stress, Sci. Rep. 5 (2015) 14812.
[51] T. Madhusudhan, H. Wang, W. Dong, S. Ghosh, F. Bock, V.R. Thangapandi, S. Ranjan, J. Wolter, S. Kohli, K. Shahzad, F. Heidel, M. Krueger, V. Schwenger, M. J. Moeller, T. Kalinski, J. Reiser, T. Chavakis, B. Isermann, Defective podocyte insulin signalling through p85-XBP1 promotes ATF6-dependent maladaptive ER-stress response in diabetic nephropathy, Nat. Commun. 6 (2015) 6496.
[52] S.W. Park, Y. Zhou, J. Lee, A. Lu, C. Sun, J. Chung, K. Ueki, U. Ozcan, The regulatory subunits of PI3K, p85alpha and p85beta, interact with XBP-1 and increase its nuclear translocation, Nat. Med. 16 (4) (2010) 429–437.
[53] J.N. Winnay, J. Boucher, M.A. Mori, K. Ueki, C.R. Kahn, A regulatory subunit of phosphoinositide 3-kinase increases the nuclear accumulation of X-box-binding protein-1 to modulate the unfolded protein response, Nat. Med. 16 (4) (2010) 438–445.
[54] A. Bettaieb, K. Matsuo, I. Matsuo, S. Wang, R. Melhem, A.E. Koromilas, F.G. Haj, Protein tyrosine phosphatase 1B deficiency potentiates PERK/eIF2alpha signaling in brown adipocytes, PloS One 7 (4) (2012), e34412.